Ultrasonics 93 (2019) 43–62

Contents lists available at ScienceDirect

Ultrasonics

journal homepage: www.elsevier.com/locate/ultras

A combined linear and nonlinear ultrasound time-domain approach for impact damage detection in composite structures using a constructive nonlinear array technique

Gian Piero Malfense Fierro, Michele Meo*

University of Bath, Materials Research, Department of Mechanical Engineering, Claverton Down, Bath, UK

ARTICLE INFO

Keywords:
Nonlinear ultrasound
Nonlinear imaging
Phased array
Laser vibrometer
Composite
Baseline-free
Defect resonance
Impact damage

ABSTRACT

Discovery and evaluation concerns of barely visible impact damage in composite materials is a well-known issue in industries using these materials. This work proposes a frequency sweep method where damage assessment is conducted with respect to the time domain. Firstly, a combined linear and nonlinear ultrasound imaging technique is proposed, which focuses on the excitation of damage/defect regions using a frequency sweep methodology from multiple transducer locations. Secondly, the method deconstructs time domain signals, which allows for the visualisation of linear and nonlinear ultrasound components independently. While, a filtering and frequency band separation method was used to exploit defect responses over different frequency ranges and provide time domain visualisation at the damage region. Finally, image segmentation was employed to automate the damage sizing procedure, while a binary imaging method was used to remove false positive damage regions produced by material vibration mode excitation (fundamental frequency responses) by using the nonlinear responses as a baseline-free tool.

The results showed that the combined linear and nonlinear results provided more accurate results than a purely linear or nonlinear approach, furthermore the results were shown to be equivalent to those of a standard phased array system. The ability of the method to visualise nonlinear outputs in time can improve the understanding of nonlinear ultrasound mechanisms while provides a clear argument that a complete approach, incorporating both linear and nonlinear methods should be regarded as the future of NDT/E systems.

1. Introduction

Carbon fibre reinforced plastic (CFRP) composite materials are currently used in a wide range of engineering disciplines, as these types of materials generally have good strength to weight capabilities. Furthermore these materials can be tailored to meet a large range of mechanical properties making them suitable for many different applications. Composite materials present a two-fold problem when evaluation of damage/defects is required as [1]: (i) the stress field associated with a typical fibre/matrix composite is essentially discontinuous thus quantitative studies on the microscopic scale are not practical, and (ii) in general composite structures are orthotropic therefore there can be markedly different mechanical properties in the three principle directions thus simple theories devised for isotropic mediums are not sufficient.

Along with the complexity of these structures they have inherent weaknesses such as susceptibility and difficulty in impact damage evaluation, which can lead to large decreases in the strength of components and can ultimately lead to failure. Low velocity impact damage can be difficult to evaluate as larger areas of delamination can be hidden under little to no surface damage, which can results in a significant drop in the materials strength. This type of damage is generally referred to as barely visible impact damage (BVID), and it can be caused during manufacturing as well as in service.

This paper focuses on the use of a semi-contact method (but is not limited to this) which utilises both linear and nonlinear ultrasound techniques to evaluate BVID in composite structures. The work develops a data acquisition and filtering methodology to extract frequency specific time data which is used to determine defect resonance and visualise the defect vibration modes.

De Angelis et al. [2] first describe a methodology for the recognition of the resonance modes of defects, a defect resonance. This is important as exciting at defect resonance results in an amplification of the defect response [3]. Defect resonance determination is a difficult and time

---

* Corresponding author at: Material Research Centre, Department of Mechanical Engineering, University of Bath, Bath BA2 7AY, UK.
E-mail address: m.meo@bath.ac.uk (M. Meo).

https://doi.org/10.1016/j.ultras.2018.10.011
Received 16 July 2018; Received in revised form 10 October 2018; Accepted 24 October 2018

consuming process thus a broadband frequency (sweep) excitation [4,5] method was used to ensure excitation of at least one defect resonance.

A constructive nonlinear array (CNA) technique was proposed by Fierro and Meo [6] for optimising nonlinear imaging (NIM) of damage in composite structures. This work looks to improve the effectiveness and reliability of this method and other damage detection techniques by combining linear and nonlinear components through time domain analysis and imaging algorithms. CNA is a post-process technique (but not limited to this) used to constructively phase match multiple captured signals at a particular position (*k*) given multiple transmit positions (*j*), similar to the standard ultrasound phased array total focusing method (TFM). The method relies on capturing the signal on the surface of the structure using a laser vibrometer (LV) while exciting from multiple locations. In this case the continuous single frequency time domain signal used by Fierro and Meo [6] is substituted with a broad frequency sweep as outlined above. This results in a prolonged ultrasonic force acting on damaged/defected regions, ultimately increasing the probability of the generation and capture of nonlinearities produced by exciting at defect resonance. This methodology ensures that both the linear and nonlinear components have increased probability of defect excitation.

A laser vibrometer (LV) was used to capture multiple signals over a grid of points while the structure was excited from multiple locations, using a frequency sweep from 20 kHz to 30 kHz (and 30–40 kHz). These captured signals were then filtered (using a high and low pass filter) and constructively phased matched to allow for time domain visualisation of the damage vibration. By filtering over the selected sub bands (20–21 kHz, 22–23 kHz, etc.) in time and phase matching each captured signal from all the array positions, time domain visualisation of the specific frequency band is possible. Following this method it is also possible to visualise higher order harmonics (nonlinear responses), i.e. at twice (40–60 kHz) and three (60–90 kHz) times the frequency of the sweep. Thus, evaluation of which sub band contained the defect resonance is possible. For the purpose of this work only ten sub bands were used, but by introducing more sub bands resolution of defect resonance would increase. As will be shown in the experimental results, there is no requirement to predetermine the defect resonance in order to evaluate damage/defects.

This work also combines linear and nonlinear results to improve damage detection and sizing. While linear techniques are well established in industry, they are not without drawbacks as with any nondestructive testing (NDT) technique. While, nonlinear ultrasound techniques have yet to be fully accepted as an alternative to standard linear approaches. Over the years many different nonlinear ultrasound approaches have been developed, these include single frequency excitation, modulation (multiple frequency mixing) and harmonic generation [7–14]. Nonlinear techniques focus on correlating the presence of additional frequency components in the output signal with damage/defects. Research into this area of ultrasonics is driven by the increased sensitivity to damage and damage evolution, predicted at a few orders of magnitude higher, while linear techniques are only sensitive to gross defects rather than micro-damage [15–17]. Ultrasonic guided waves inspection methods, based on the analysis of material nonlinear elastic effects, have been developed for the detection and localisation of structural defects. These defects include, micro-cracks (fatigue), delaminations, weak adhesive bonds, and more [18,19]. Some of the most well-known nonlinear techniques include nonlinear elastic wave spectroscopy (NEWS) [20–22], nonlinear elastic wave modulation spectroscopy (NEWMS) [23,24], nonlinear imaging methods [25,26], and phase symmetry analysis (PSA) techniques [27,28].

Nonlinear ultrasound phased array techniques were assessed by the following authors [29–32]. Ohara et al. [30] and Park et al. [32] have extensively developed and evaluated and improved the detection of open and closed cracks in metallic structures using a subharmonic phased array, while Potter et al. [31] has developed a nonlinear array based on the traditional TFM. These methods provide nonlinear ultrasound information through the thickness of the sample, rely on short excitation signals, have been assessed on metallic structures and do not generally address issues of equipment based nonlinearities. Furthermore, nonlinear ultrasound techniques generally focus on frequency domain evaluation and assessment to determine damage/defects, Boccardi et al. [10] suggests a time domain approach for defect localisation based on the time of arrival (ToA) of the nonlinear signal but this did not include damage imaging.

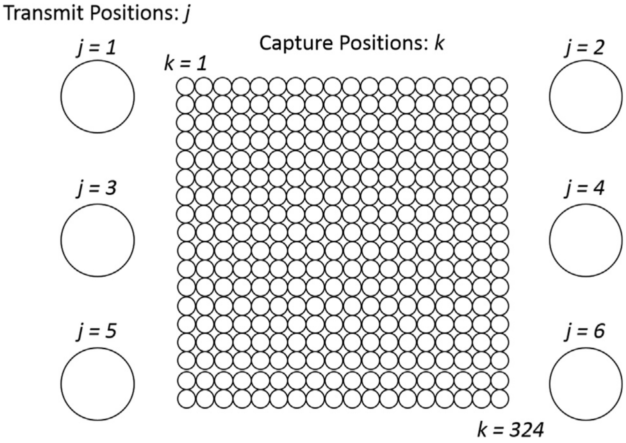

Fig. 1. Example of transmit positions (*j*) and capturing positions (*k*).

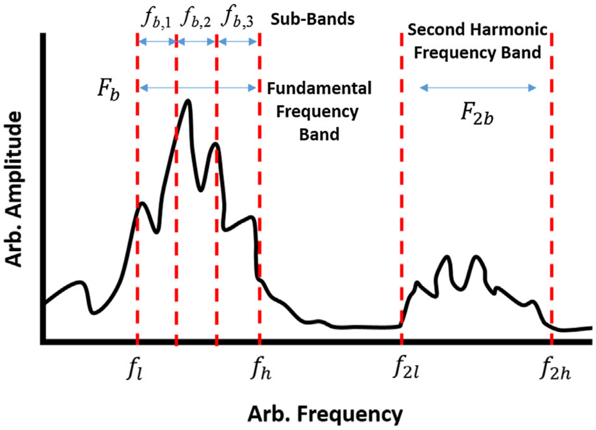

Fig. 2. Frequency Band Selection.

Some of the most promising non-destructive testing methods are arguably thermography, non-contact laser ultrasonic and air-coupled ultrasonic techniques. Thermosonics has attracted a large amount of attention due its rapid deployment and ease of use. In thermosonics, a medium is excited using a piezoelectric transducer (PZT) or welding horn where damage is evaluated by processing the thermal response with an infrared (IR) camera [33]. These methods have issues of: repeatability due to the physics governing the heat generation process in vibrating defects, are limited to thinner structures, and correct excitation frequency determination. Recent work in this field has focused on excitation at local defect resonance, long pulse and lock-in techniques [34] and the utilisation of a sweep excitation methodology to ensure defect excitation [35].

Non-contact laser ultrasonic methods use lasers to generate and receive ultrasonic waves have been shown to provide equivalent results when compared to conventional ultrasound techniques [36–38]. While these methods have shown good results, non-contact laser systems are very expensive and rely on single point excitation and capture. Air-coupled ultrasonic methods using air-coupled transducers have been extensively studied and shown reliable results in damage detection

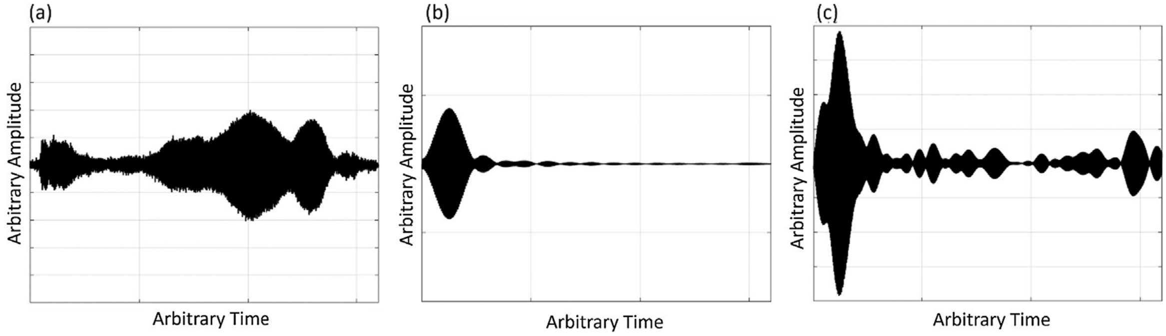

Fig. 3. Raw captured signal (a), filtered fundamental sub band signal (b) and filtered second harmonic sub band signal (c).

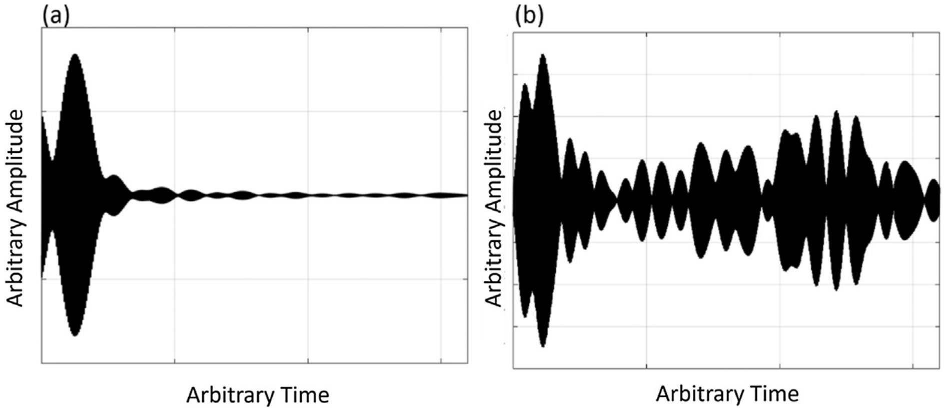

Fig. 4. Sum of all filtered fundamental sub band signals (a) and sum of all filtered second harmonic sub band signals (b) for all excitation locations *j*.

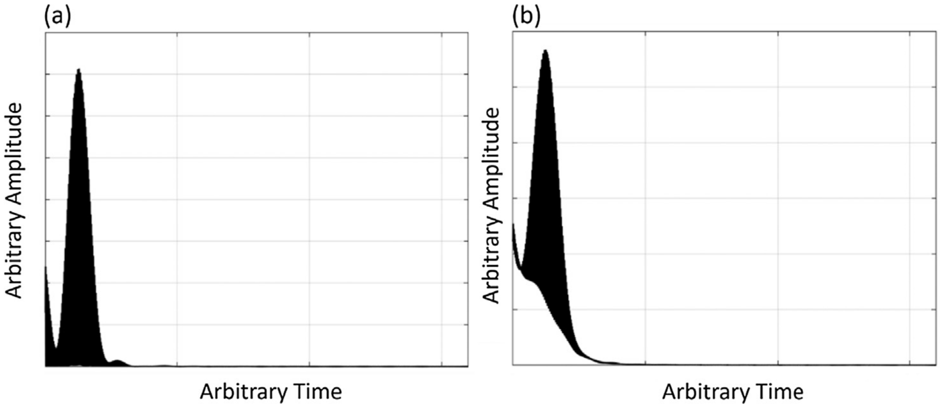

Fig. 5. Arbitrary Energy (V2) of a single point (a) and total energy per frame (b).

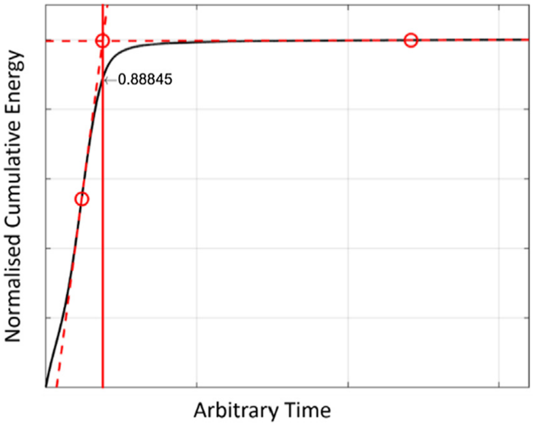

Fig. 6. Normalised Cumulative Energy and time selection point.

[39–42]. Although due to the large impedance mismatch between air and composite materials low amplitude excitation of these structures is generally achieved, this reduces potential to observe wave-defect interactions in the captured signals and thus reduces damage/defect detectability. Other composite damage imaging techniques include ground penetrating radar [43], terahertz spectroscopy [44], X-ray computed tomography [45] and electrical techniques [46]. These methods have shown accurate results, but have limitations such as: material, portability and adaptation for field work. This work provides the first nonlinear ultrasound focused time domain visualisation of the nonlinear vibration of a damage/defect, and thus will be referred to as the Constructive Nonlinear Array in Time (CNAT).

Using an image segmentation (IS) technique to automate the evaluation of damage regions it is possible to directly compare the ability of linear responses to assess damage regions versus areas determined using the nonlinear responses. The experimental results clearly show

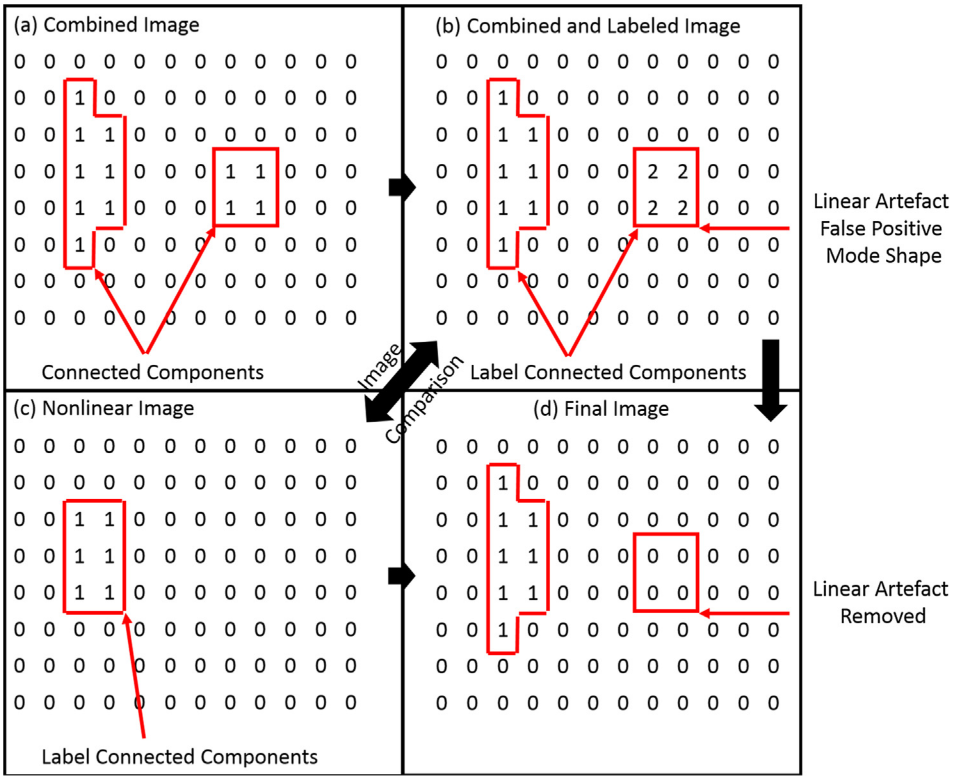

(a) Combined Image

0	0	0	0	0	0	0	0	0	0	0	0
0	0	1	0	0	0	0	0	0	0	0	0
0	0	1	1	0	0	0	0	0	0	0	0
0	0	1	1	0	0	0	1	1	0	0	0
0	0	1	1	0	0	0	1	1	0	0	0
0	0	1	0	0	0	0	0	0	0	0	0
0	0	0	0	0	0	0	0	0	0	0	0
0	0	0	0	0	0	0	0	0	0	0	0

(b) Combined and Labeled Image

0	0	0	0	0	0	0	0	0	0	0	0
0	0	1	0	0	0	0	0	0	0	0	0
0	0	1	1	0	0	0	0	0	0	0	0
0	0	1	1	0	0	0	2	2	0	0	0
0	0	1	1	0	0	0	2	2	0	0	0
0	0	1	0	0	0	0	0	0	0	0	0
0	0	0	0	0	0	0	0	0	0	0	0
0	0	0	0	0	0	0	0	0	0	0	0

(c) Nonlinear Image

0	0	0	0	0	0	0	0	0	0	0	0
0	0	0	0	0	0	0	0	0	0	0	0
0	0	1	1	0	0	0	0	0	0	0	0
0	0	1	1	0	0	0	0	0	0	0	0
0	0	1	1	0	0	0	0	0	0	0	0
0	0	0	0	0	0	0	0	0	0	0	0
0	0	0	0	0	0	0	0	0	0	0	0
0	0	0	0	0	0	0	0	0	0	0	0

(d) Final Image

0	0	0	0	0	0	0	0	0	0	0	0
0	0	1	0	0	0	0	0	0	0	0	0
0	0	1	1	0	0	0	0	0	0	0	0
0	0	1	1	0	0	0	0	0	0	0	0
0	0	1	1	0	0	0	0	0	0	0	0
0	0	1	0	0	0	0	0	0	0	0	0
0	0	0	0	0	0	0	0	0	0	0	0
0	0	0	0	0	0	0	0	0	0	0	0

Fig. 7. Binary Image Processing: combined linear and nonlinear damage image (a), labelling of separated damage region (b), nonlinear damage image (c), and image after binary image processing and removal of linear artefact (d).

that while both methods can clearly determine the damage region the size and shape of these regions differ. Generally in all cases, there are regions that are predicted by the linear as damage that are not predicted in the nonlinear case and *vice versa*. This adds a strong argument to combine the two methods and generate a single linear and nonlinear image. This work develops a highly repeatable methodology for the processing, merging and validation of damage/defects. The IS technique is run to a predetermined cut-off point, which relates to an cumulative energy value for that particular band, thus setting a threshold on the information in the time domain signal that is used to evaluate the damage (this will be discussed in further detail in the next section). Using this methodology a linear and nonlinear damage image is generated and then combined to create the final damage image.

Through experimentation it was found that in certain cases artefacts within the linear images did not correspond to damage locations but were in fact due to mode shapes over the excitation sub band. Thus to further improve and remove false positives from the final results a binary imaging (BI) process was used to compare the nonlinear image with the combined image. Any artefact that did not relate to a region found by the nonlinear method was considered a false positive and removed from the final image of the damage region. The reason for this was that nonlinear responses only exist in the presence of damage, this was clearly observed in the experimental results, which showed an improvement in accuracy of the damage size after BI was conducted when compared to standard phased array results.

A simple analytical model was developed to evaluate the potential error in damage sizing due to the pitch between elements (i.e. pixel size of the captured data), the model showed that the results obtained using the CNAT method with lower resolution, less captured points over an area than a standard phased array system, provided equivalent error margins on damage sizing, while showing that one of the limiting factors was the pitch size. Two of the main benefits of the method were that it allowed excitation at lower frequencies (under 100 kHz, unlike standard phased arrays) and used less excitation locations which is possible due to the longer excitation signal and lower attenuation of the signal at these lower frequencies. Furthermore, by combining both the linear and nonlinear results more accurate damage sizing was obtained than by concentrating on linear or nonlinear results separately. The method was also semi-contact (potential for fully non-contact) and thus eliminates some of the issues with contact methods such as consistent coupling, near-field resolution and requirements for physical scanning.

2. Constructive interference, data acquisition, filtering, image segmentation and binary image processing

2.1. Constructive interference

This work builds on work completed by Fierro and Meo [6] which describes a constructive nonlinear array (CNA) technique for optimisation of nonlinear imaging (NIM) of composite structures. The CNA method relies on a post-process technique (but not limited to this) used to constructively phase match multiple captured signals at a particular position (k) using a laser vibrometer (LV) given multiple transmit positions (j) using a piezoelectric transducer (see Fig. 1).

Assuming that time domain signal with a certain frequency (f) can be represented as $f_{j,k}(t)$, the sum and phased matched signal for two transmitting elements at receiving position k can be defined by the below equation:

$$F_{2,k} = \max\left(\left\{\int_0^T abs((f_{1,k}(t) + f_{2,k}(t+\Delta t_1)))dt, \ldots, \int_0^T abs((f_{1,k}(t) + f_{2,k}(t+\Delta t_n)))dt\right\}\right) \tag{1}$$

where F is the constructive matched signal for the selected frequency, with Δt_n being the phase lag. Maximum constructive interference occurs within one period shift (T_p, time to complete n periods calculated by $n\cdot(1/f)$ with $n = 0, 1, 2 \ldots$) of two signals with a total time (T), assuming a frequency of f. The above equation was used to phase-match multiple

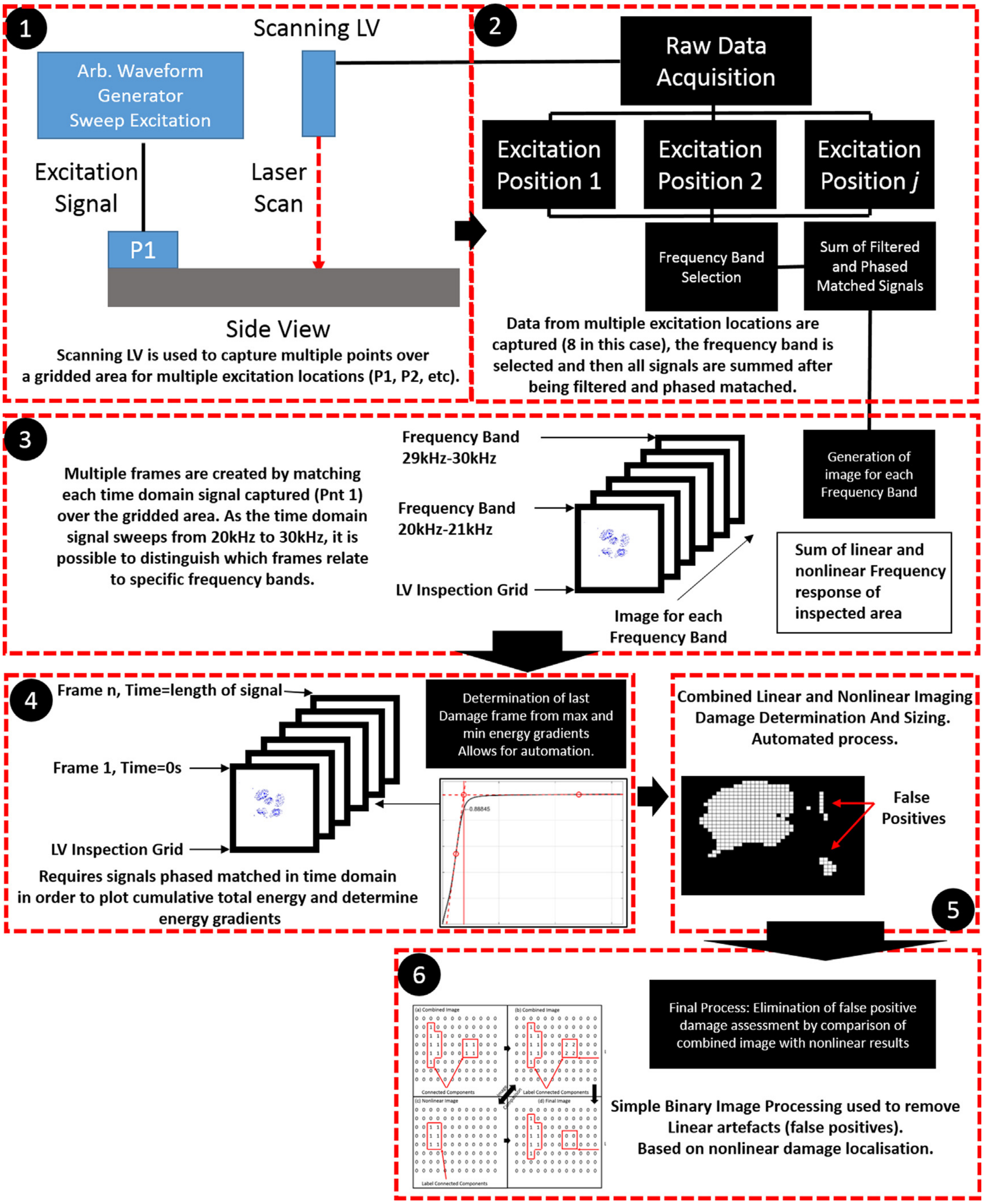

Fig. 8. Summary of Experimental Setup and Signal Processing.

excitation location signals.

The technique proposed by Fierro and Meo [6] was equivalent to adding all harmonic component amplitudes gathered from the fast Fourier transform (FFT) of each transmitted signal location. This process can be completed in the frequency domain without consideration to the phase matching process that was outlined. This work develops a time domain process that focusing on visualising harmonic responses both linear and nonlinear. Time domain analysis provides greater detail in terms of damage response to the excitation frequency and allows for the visualisation and evolution of this response in time. The difficulty lies in distinguishing between material and damage responses when exciting at various frequencies, which makes robust damage assessment dependent on correct frequency selection i.e. defect resonance.

2.2. Data acquisition and filtering

This work proposes a methodology that focuses excitation over a broad frequency band (sweep excitation), with the intent of increasing the probability that defect resonance will be excited. Furthermore, in order to evaluate defect/damage responses at various frequencies, smaller frequency bands (sub bands) were created. This was done by dividing the broad frequency band into smaller bands, increasing the probability of accurately determining the defect resonance frequency (shown experimentally). The sub bands over the range are generated by using a band-pass filter between the required frequency bands in order to keep the time domain history of the response. For example: a broad band frequency excitation was conducted between 20 kHz and 30 kHz and sub divided into 10 frequency bands of 1 kHz each (i.e. 20–21 kHz, 21–22 kHz, etc.). In addition to the fundamental frequency sub bands,

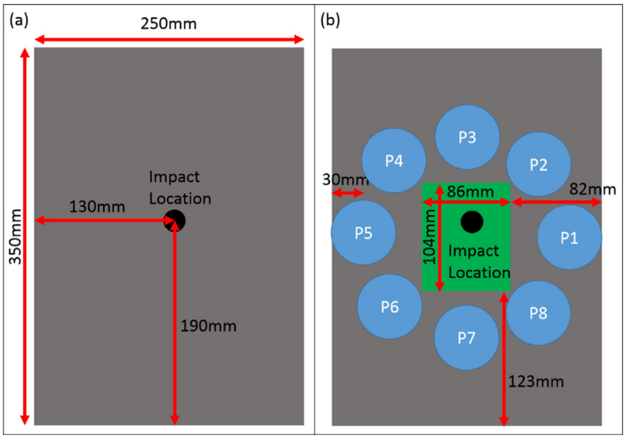

Fig. 9. Flat panel impact location and panel dimensions (a), and transducer and LV grid setup (b).

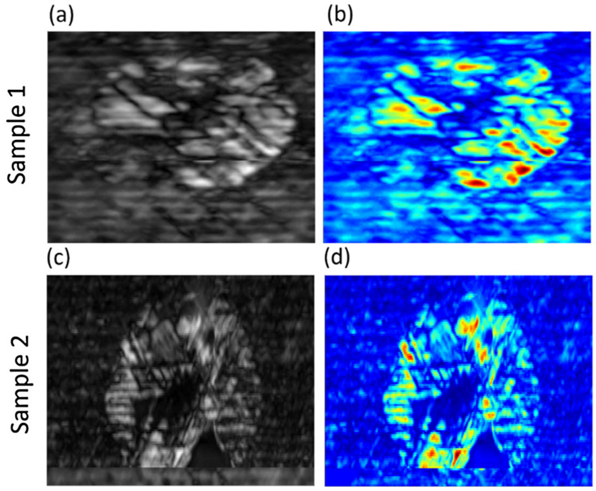

Fig. 10. Impact damage for S1 and S2 – standard phased array amplitude results in grey (a) and (c) and coloured maps (b) and (d).

Table 1

Frequency sweeps conducted for each sample and sub band selection.

Sample	Sweep	Band no.	Fundamental Sub bands (10 bands)	Second Harmonic Sub bands (10 bands)
S1&S2	20–30 kHz	B1	20–21 kHz	40–42 kHz
		B2	21–22 kHz	42–44 kHz
		B3	22–23 kHz	44–46 kHz
		B4	23–24 kHz	46–48 kHz
		B5	24–25 kHz	48–50 kHz
		B6	25–26 kHz	50–52 kHz
		B7	26–27 kHz	52–54 kHz
		B8	27–28 kHz	54–56 kHz
		B9	28–29 kHz	56–58 kHz
		B10	29–30 kHz	58–60 kHz
S2	30–40 kHz	B11	30–31 kHz	60–62 kHz
		B12	31–32 kHz	62–64 kHz
		B13	32–33 kHz	64–66 kHz
		B14	33–34 kHz	66–68 kHz
		B15	34–35 kHz	68–60 kHz
		B16	35–36 kHz	60–62 kHz
		B17	36–37 kHz	62–64 kHz
		B18	37–28 kHz	64–66 kHz
		B19	38–39 kHz	66–68 kHz
		B20	39–40 kHz	68–60 kHz

second harmonic sub bands were also investigated by filtering at twice that of the fundamental sub bands (i.e. 40–42 kHz, 42–44 kHz, etc.). These bands are described in Fig. 2 below where: F_b refers to the fundamental frequency band excitation frequencies with b being the frequency band number, F_{2b} refers to the second harmonic frequency band which is twice that of F_b, f_l and f_h are the lowest and highest frequency in the sweep respectively, with multiples of these frequencies giving the second (f_{2l} and f_{2h}) frequency bands. Thus the frequency response of each band can be calculated as follows:

$$F_b = \int_{f_l}^{f_h} F(f)df;\ F_{2b} = \int_{f_{2l}}^{f_{2h}} F(f)df \tag{2}$$

Fig. 3 below shows the raw time domain signal along with the filtered fundamental and second harmonic responses for an individual excitation (j) and capture (k) position.

In order to determine the summed time domain data for each excitation position (j) for a given capture position (k), each captured response needs to be phased matched according to Eq. (1). In this case phase matching was conducted as a post-process step (but is not limited to this), Fig. 4 shows the summed time domain signals for a given number of excitation locations (8 in this case). Due to the anisotropic nature of composite materials and defects/damages the location of excitation has an influence on the response at a given capture position (k), adding to this is the attenuation of the excitation signal from the source.

The difficulty in any image processing algorithm and an automated algorithm to determine damage size is what information from the raw signal is essential to accurately determine the damage size, while being repeatable. Thus the focus of this work was to develop a framework, first for conducting the test itself and then for analysing the raw data. In order to do so, it is important to establish set parameters (mathematical or statistical). From the summed sub band signals it is possible to determine the energy (Fig. 6, V^2) of each captured position (k) in time, and then calculate the total energy (the sum of every captured position (k)). By plotting the energy of each point frame by frame it is possible to evaluate the areas of maximum energy through time, with the expectation that the areas relating to the maximum energy would correspond to the damage region (due to the reduction in stiffness in this area) or a material resonance. This allows for the generation of frequency selective images for each point in time (a video of the frequency band response), with novelty being the visualisation in time of higher order harmonics (the second harmonic in this study). What is expected, is that while it is known that the fundamental is key in exciting the damage region it can excite both material and damage/defect resonances making damage determination difficult, while the production of the second harmonic should only be evident at damage regions. Thus, the nonlinear behaviour becomes an important tool of the damage sizing algorithm as it can be used as the determining factor of whether fundamental responses are material or defect related, providing an improvement on the validation of results.

2.3. Image segmentation and binary image processing

The image algorithm employed was a combination of two simple known methods, the first an image segmentation (object detection) method (IS) generally used for biological cell determination, and a Binary Image (BI) method to compare the linear and nonlinear images against each other (using MATLAB R2014b functions "*edge*" and "*Sobel*" operators used for IS, and "*bwconncomp*" for BI). The IS method used a Sobel edge detection method to generate a binary gradient mask, the image is then dilated with the interior gaps being filled to generate a solid area. The difficulty in using this method is that as the signal to noise ratio (SNR) reduces towards the end of the sub band, larger and larger areas become classified as objects within the image (i.e. the damage becomes larger and larger). Thus a cut-off point is required in order to ensure that results are a true reflection of the damaged state of

Table 2
Variables and description of analytical model.

	Variable:	Area calculation:	Assuming N = 1 (Fig. 11)	General assumptions:
1.	Overestimate area	$(2N+1)^2{*}Pitch$	Area of outer box ADotted black box.	● Square Damage Area ● Worst case scenario, ● Damage region can only be observed if capture position is directly above location ● Limiting factor is distance between pitch ● Stepped-Linear Phased Array
2.	Actual damage area	$(2N)^2{*}Pitch$	Area of middle box BDotted red box.	
3.	Underestimate area	$(2N-1)^2{*}Pitch$	Area of inner box CSolid black box.	
4.	Percentage error underestimate	$\frac{-4N+1}{4N^2}$	Difference between box B and C	
5.	Percentage error overestimate	$\frac{(2N+1)^2}{4N^2}-1$	Difference between box A and B	
6.	Optimum damage area	$(2N)^2{*}Pitch$	Capture locations positioned at points 10 to 13	

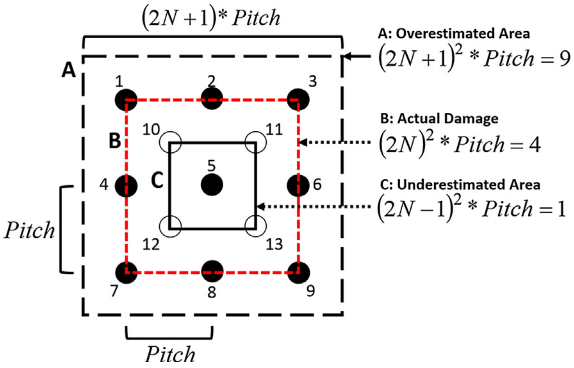

Fig. 11. Analytical model representation for $N = 1$ and $Pitch = 1$, for an over (dotted black box A) and underestimated (solid black box C) damage (dotted red box B) regions.

the material. By calculating the cumulative energy (Fig. 6) from the total energy (Fig. 5), and then determining the time of the intersection between the highest and lowest gradient points a framework for selecting this cut-off point was generated. For example in Fig. 6, given the cumulative energy curve, this point in this case occurs at 88.8% of the total energy and at a time (t). The percentage of total energy is not a constant in this case and changes according to the cumulative energy profile of each sub band.

Furthermore, as the time domain is used, selecting a single frame/response at the cut-off point would not necessarily capture the full extent of the damage. This is due to the fact that defect resonance over a short sub band frequency range could excite different locations within the damage area, which was clearly evident in the visualisation of the damage in time (this will be discussed in the results). Therefore, the IS method was conducted for each frame from the first to the cut-off point and then each image was added to generate a single image of the damage region.

As this work focuses on multiple aspects of damage assessment from damage evaluation algorithms to combining both linear and nonlinear methods to provide improved damage assessment. The IS results for the fundamental and second harmonic responses were combined to generate a single image of the damage. In order to ensure that material mode responses were not evaluated as damage, a simple BI method was employed. If the combined image linear and nonlinear image is considered and is converted into zeros and ones (Fig. 7(a)), two damage regions have been determined using the IS process. If each region is now numbered (1 and 2, Fig. 7(b)) there are two damage regions. If the combined image (Fig. 7(b)) is compared to the nonlinear image (Fig. 7(c)) it is clear that the damage labelled 2 is a false positive, on the assumption that: nonlinearities are only present at damage locations while fundamental responses will be present throughout the surface of the composite (material modes) and at the damage region. Thus by eliminating any response labels that cannot be found in the nonlinear image (i.e. 2), a final image (Fig. 7(d)) only containing damage/defect responses can be determined.

2.4. Summary of method

As this work builds on the Constructive Nonlinear Array (CNA, [6]) technique it will be referred to as the Constructive Nonlinear Array in Time (CNAT) for the purposes of this paper. CNAT can be broken down into 6 main steps, refer to Fig. 8 below.

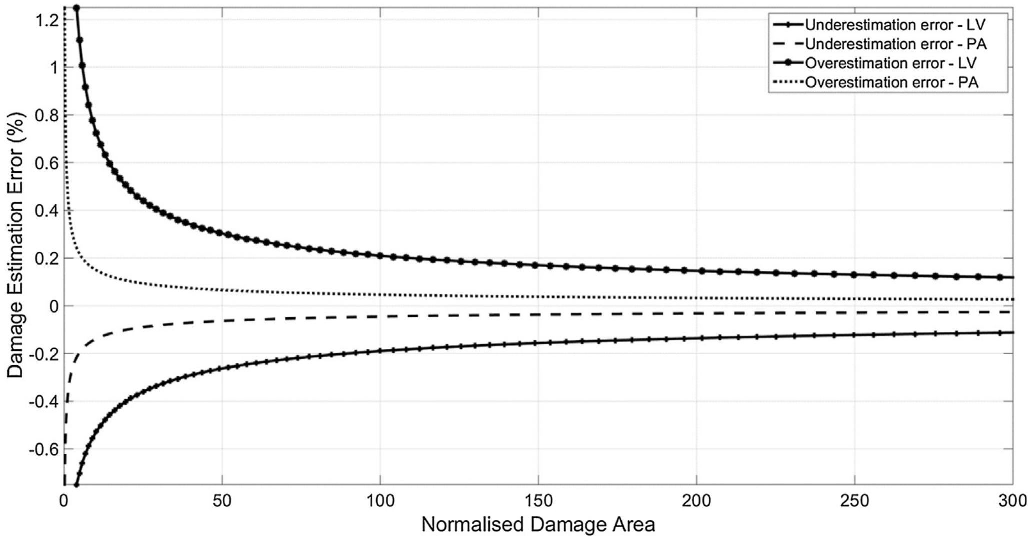

Fig. 12. Analytical model representation for N = 1–300 and $Pitch$ = 1.

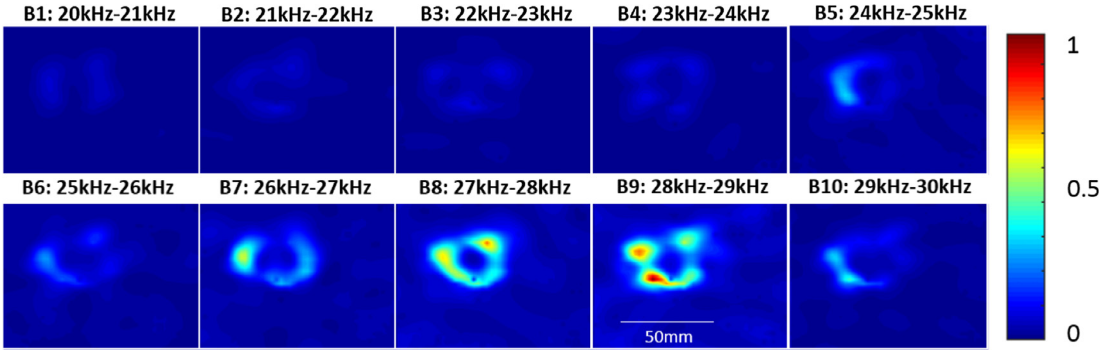

Fig. 13. Comparison of total energy for each frequency sub band for the fundamental frequency normalised to maximum of all frequency bands S1.

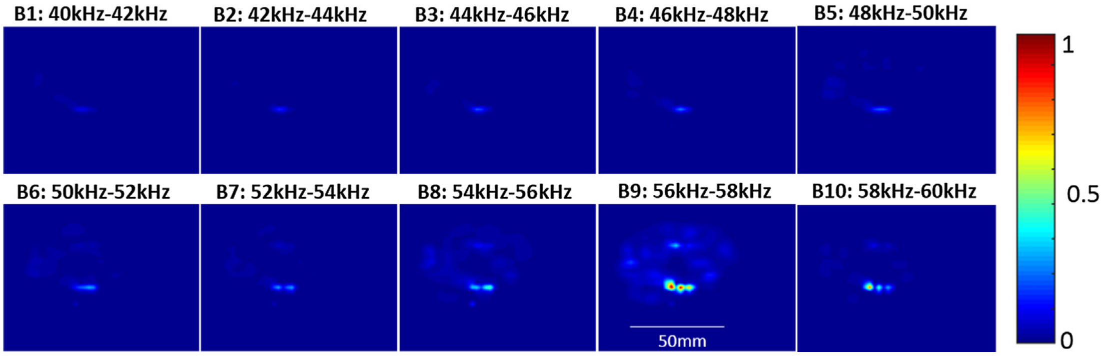

Fig. 14. Comparison of total energy for each frequency band for the second harmonic normalised to maximum of all frequency sub bands S1.

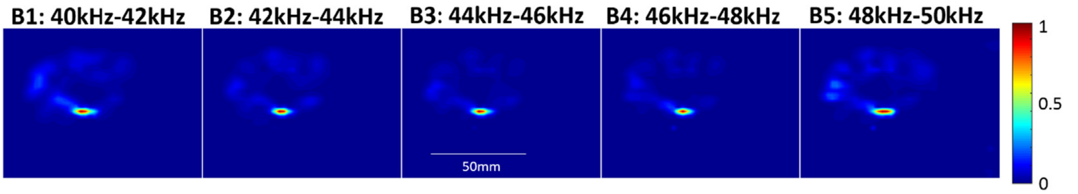

Fig. 15. Comparison of total energy for frequency sub bands B1 to B5 (left to right) for the second harmonic, normalised for each image S1.

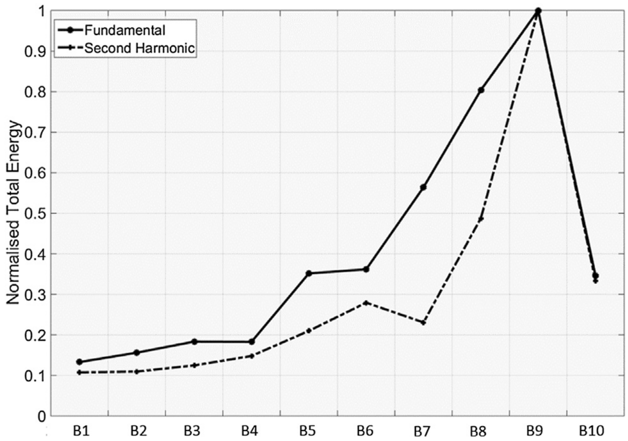

Fig. 16. Comparison of total energy for each frequency band for the fundamental and second harmonic S1.

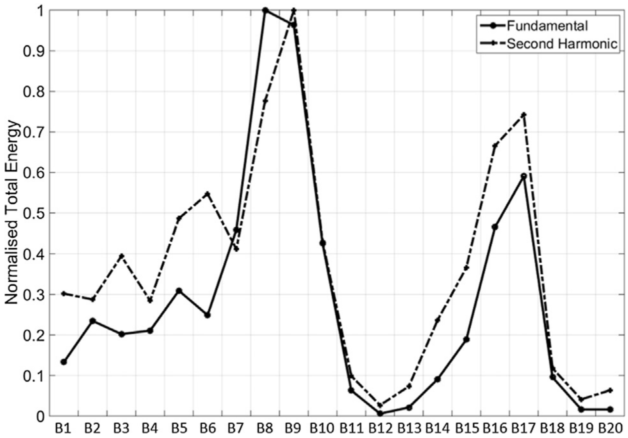

Fig. 17. Comparison of total energy for each frequency band for the fundamental and second harmonic S2.

1. Sample setup and layout: which uses a piezoelectric transducer to excite at multiple locations and a laser vibrometer (LV) to capture.
2. Data Acquisition: collection of raw data from each excitation location, frequency band selection and summing of phase matched signals.
3. Visualisation of Linear and Nonlinear Responses: imaging of each frequency band in time.
4. Image processing: determination of signal cut-off point and image segmentation based on that cut-off point.
5. Linear and Nonlinear Imaging (LNIM): combination of both linear and nonlinear imaging methods.
6. Final Image processing step: comparison between linear and

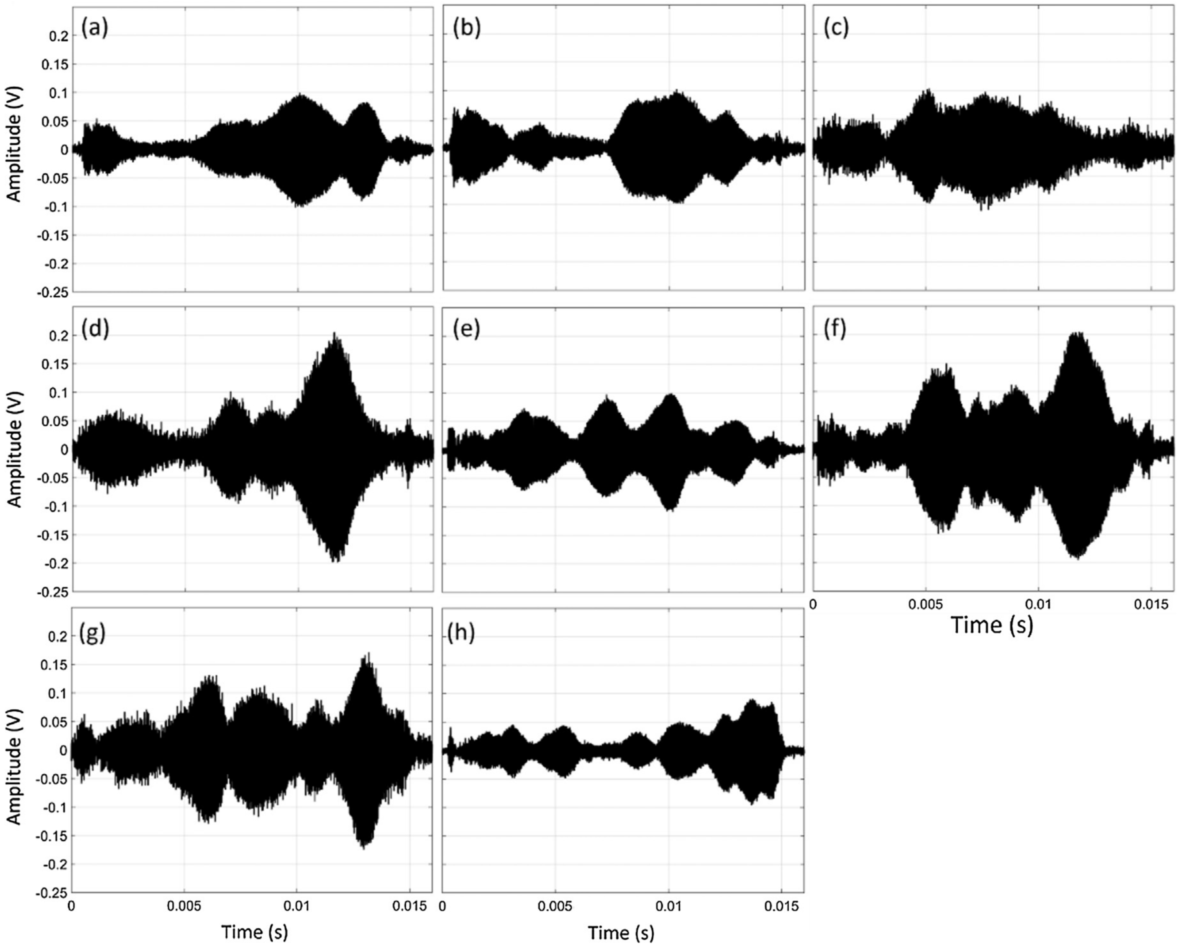

Fig. 18. Raw Time Domain signals captured at location $k = 1$ when exciting from locations $j = 1$ to $j = 8$, (a) to (h) respectively for S1.

nonlinear imaging results using binary imaging to determine false positive damage results.

3. Equipment and experimental setup

The proposed methodology was tested on two impacted composite flat plates with barely visible impact damage (BVID). The two flat plates (S1 and S2 - Fig. 9) had a width of 250 mm, length of 350 mm and thickness of 13 mm. S1 was impacted slightly of center as shown in Fig. 9, while S2 was impacted in the center of the panel. The green highlighted regions (Fig. 9) show the LV grid layout position and size relative to the samples tested. S1 and S2 was tested using 8 transmit locations (Fig. 9(b)). It should be noted that for this testing method the composite material layups/properties and impact information is considered to be unknown, in order to represent a real life scenario.

The input signals were generated using a function generator (built in generator - Polytec PSV-A-420) linked to an amplifier (Falco Systems, DC to 5 MHz, High Voltage WMA-300, x50 gain up to 300 V), and applied to the structure at 200 V with a piezoelectric active transducer (Piezoshaker PS-X-03-6/1000, central frequency of 60 kHz). The piezoelectric active transducer had a built in suction cup and was attached with the aid of a pump, with contact aided using ultrasound coupling gel. The direct out-of-plane vibration responses were captured with no averages being taken using a highly sensitive LV (Polytec PSV-A-420).

S1 and S2 had a grid size of 1665 points (37 × 45, pitch between points ~ 2.3 mm). The 8 transmit setup had a circular pattern with transducers placed at 45 degrees to one another. The signal response at each grid location was measured with a sampling frequency of 512 kHz, with the generated signal being 16 ms and 8192 points in length for both samples tested. Only one transducer was used to conduct the tests, this was done by moving the transmit position from $P = 1$ to 8.

A standard phased array (PA) system was used to evaluate the BVID in the tested samples. A 5 MHz 128 element probe (pitch ~ 0.5 mm) using beams of 32 elements was used to evaluate the samples. Fig. 10 and show the amplitude results (in grey scale and coloured map) results for S1 and S2.

A broad frequency sinusoidal sweep waveform was generated (10 kHz band) and used to excite the damage regions. The baseline free methodology adopted required that no preliminary testing to determine the excitation frequency was conducted. Rather, frequency sweeps between various ranges were conducted and acted as the initial and final BVID testing for the samples. Table 1 below highlights the test carried out for this study as well as the sub bands used.

Sweeps were conducted at intervals of 10 kHz (i.e. from 20 kHz to 30 kHz) for the eight transducer transmit setup. This was done in order to ensure that there was no overlap between the fundamental frequency response and that of the higher order harmonics. For example: the second harmonics of a sweep between 20 kHz and 30 kHz would appear between 40 kHz and 60 kHz. The excitation frequency band was chosen according to the best response (largest amplitude over the frequency range) generated by the transducer which fell between 20 kHz and 80 kHz. As the method does not rely on finding defect resonance frequencies, the testing procedure is simplified by selecting these frequency bands, while the probability of exciting at defect resonance frequency is improved.

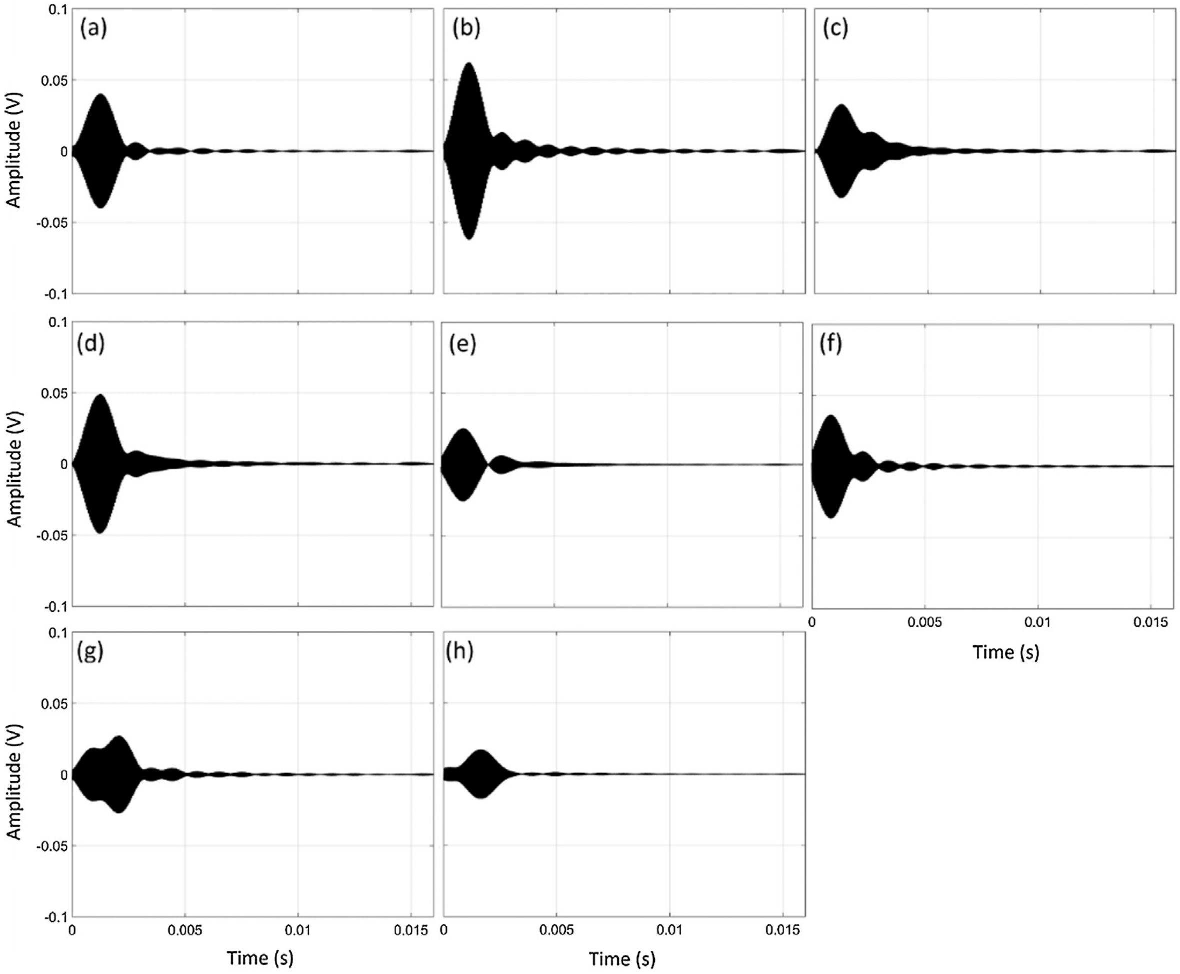

Fig. 19. Filtered Time Domain signals for fundamental sub band B1 (20–21 kHz) captured at location $k = 1$ when exciting from locations $j = 1$ to $j = 8$, (a) to (h) respectively for S1.

4. Analytical model

In order to evaluate the accuracy of the proposed CNAT method, results were compared to standard phased array (PA) from the same area. Direct comparison of the results is not possible as there are two main differences between the experimental setups: (1) element pitch distance between LV capture positions and elements along array probe and (2) the number of transmitting elements (8 used for LV and 128 for PA) which determines the ability of the method to excite damage regions. If these factors are considered, the CNAT method collected data from one point per 5.29 mm^2 (pitch of 2.3 mm × 2.3 mm) while the PA collected 19 points of data in the same area, thus has 19 times the resolution. Furthermore, the PA utilises 128 transmitting elements using multiplexed sections of 32 elements per beam (total of 97 beams), while the CNAT method only employed 8 individually transmitting elements. Please note for the purposes of this comparison various assumptions and simplifications have been made, for example it is assumed that direct line of sight is required to visualise the damage region.

One of the proposed advantages of CNAT is the use of less transmit locations, by exciting the structure with a prolonged lower frequency ultrasonic force (longer excitation signal), ultimately increasing the probability of the generation and capture of linear and nonlinear effects produced by exciting damage regions. Therefore, resolution becomes the inhibiting factor that needs to be addressed for a direct comparison between the methods.

Thus, for direct comparison of the results, a simple analytical model was used to evaluate the potential reduction in measured damage area related to the pitch (i.e. resolution differences) between capturing elements. Table 2 outlines the general assumptions of the analytical model, while Fig. 11 illustrates the model for a scenario where $N = 1$ and $Pitch = 1$. A square damage area and grid was used with multiple capture locations and assumption that the pitch between elements is the limiting factor for damage detection.

The model assumes a damage area of $(2N)^2{*}Pitch$ and $(2N + 1)^2$ capture locations ($N = 1$ to ∞), with three possible damage estimation states: (1) overestimation of damage area (Table 2 row 1, Fig. 11 capturing at locations 1–9), (2) underestimation of damage area (Table 2 row 3, Fig. 11 capturing at locations 1–9) and (3) optimum damage area (Table 2 row 6, Fig. 11 capturing at locations 10–13). For the underestimation state, it is assumed that the damage area falls within the dotted box (Fig. 11) thus capture positions 1–9 (excluding 5) do not capture damage and thus theoretically the percentage error tends to$(-4N + 1)/4N^2$.

If $N = 1$ and $Pitch = 1$ (Fig. 11) there is and underestimate of the damage size of 75% and an overestimate of 125%. As the damage area is increased there is a reduction in error in both cases, this is shown in Fig. 12 below.

5. Results and discussion

5.1. Constructive nonlinear array (CNA): Frequency domain

The frequency responses for each sub band was calculated by

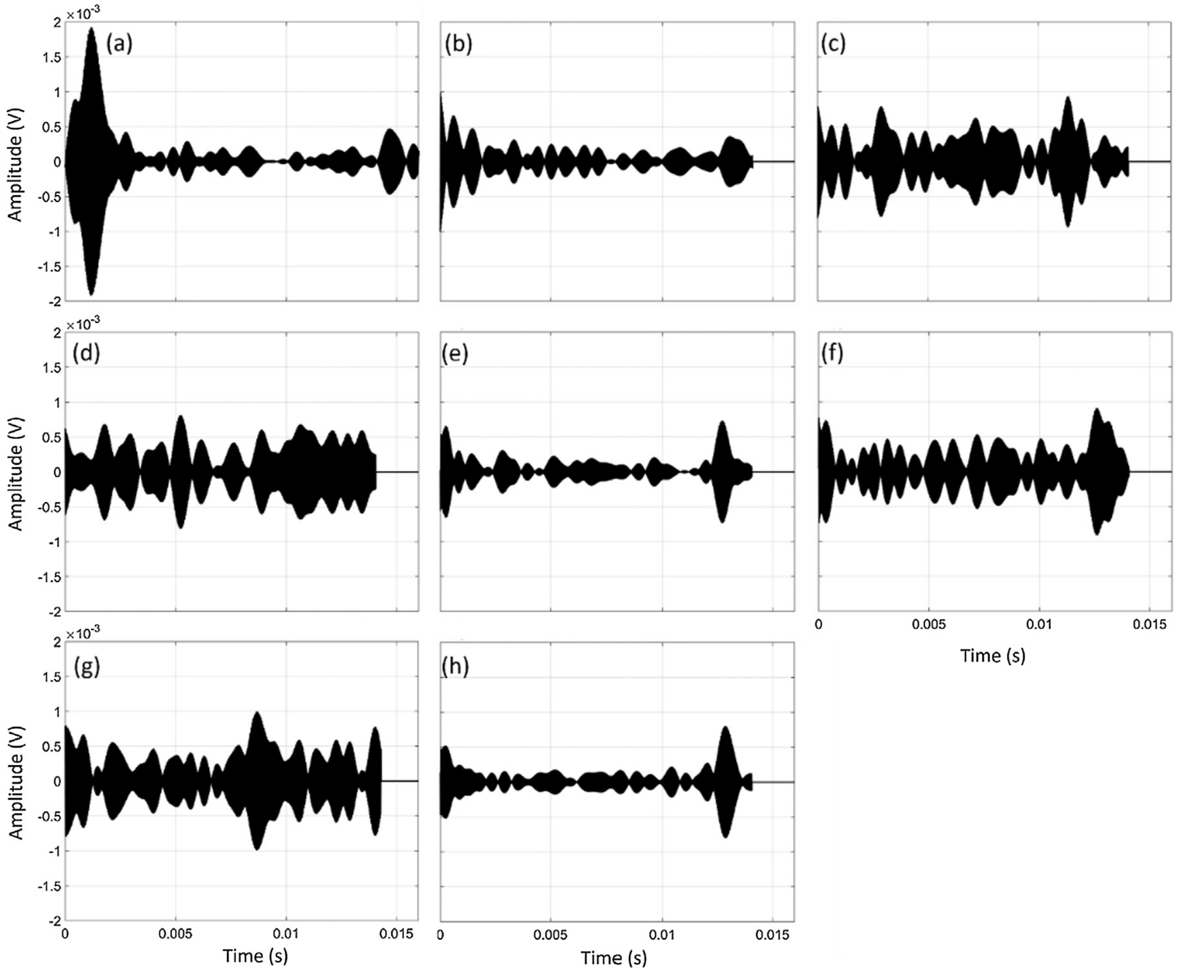

Fig. 20. Filtered Time Domain signals for second harmonic sub band B1 (40–42 kHz) captured at location $k = 1$ when exciting from locations $j = 1$ to $j = 8$, (a) to (h) respectively for S1.

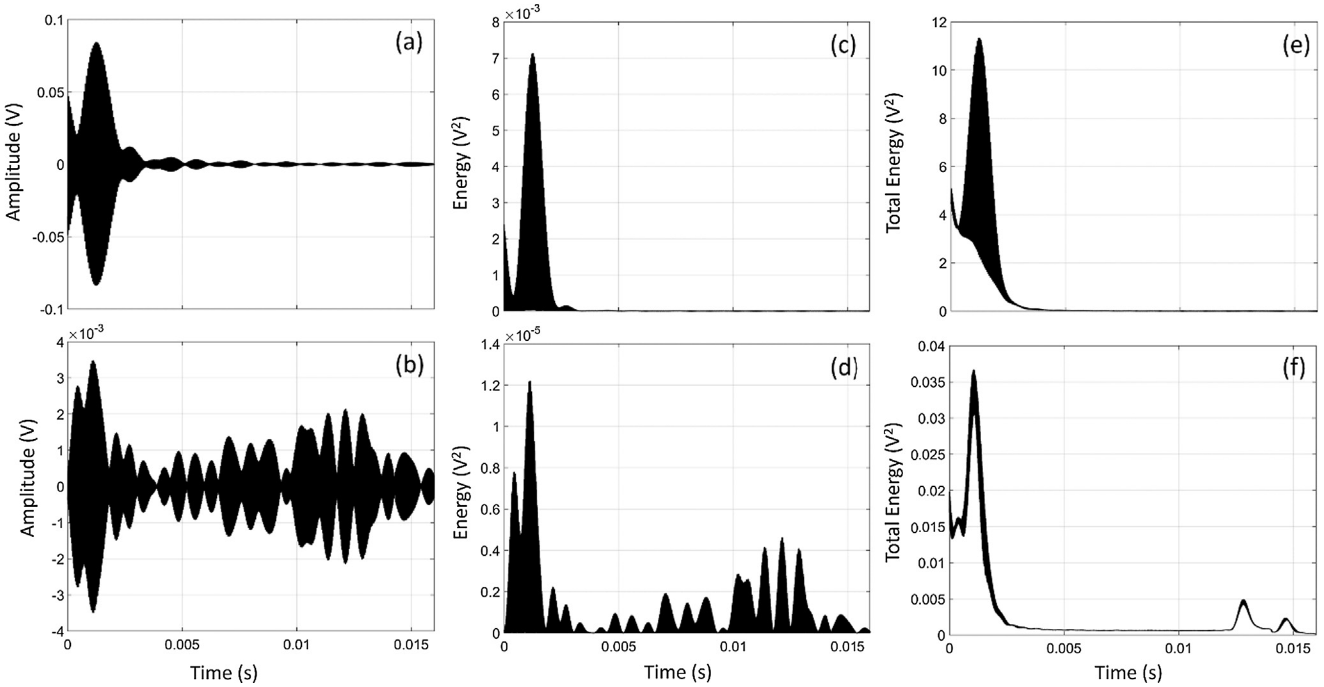

Fig. 21. Sum of Filtered Time Domain signals for the fundamental (a) and second harmonic response (b), Energy for location $k = 1$ for the fundamental (c) and second harmonic responses (d), Total Energy, sum of all k locations and j excitation locations for the fundamental (e) and second harmonic (f).

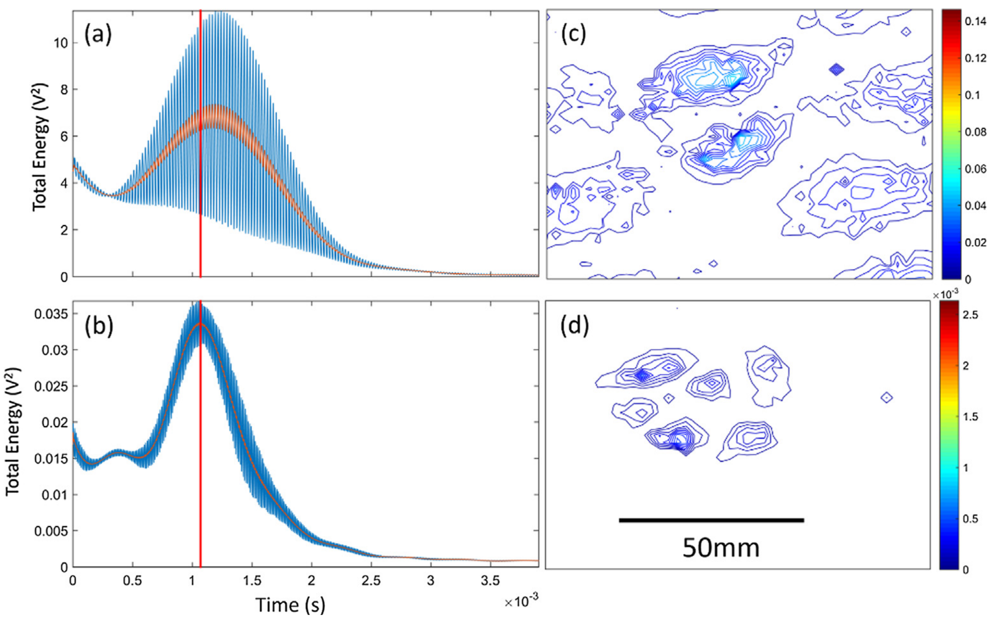

Fig. 22. Fundamental (a) and Second harmonic (b) total energy profile vs. filtered and phase matched image at 0.0011 s (c-Fundamental, d-Second) for B1 (S1: 20–21 kHz).

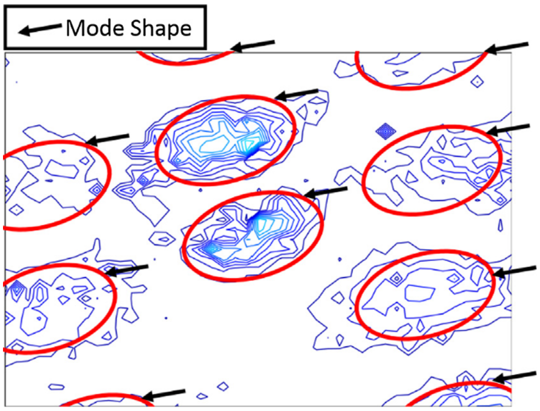

Fig. 23. Fundamental phase matched image at 0.0011 s, Mode Shapes – B1 (S1: 20–21 kHz).

integrating over each band in a similar manner to Eq. (2). Figs. 13 and 14 show the results for the fundamental and second harmonic responses as outlined in Table 1, respectively. An unweighted linear least-squares regression was used to smooth the raw data (using MATLAB function '*sgolay*'), this method is a generalised moving average with filter coefficients and a polynomial model of a specified degree (set to 4 in this case). Both images have been normalised to 1, which corresponds to the highest value of all the bands for the fundamental and second responses. In both images it is clear that the greatest response occurs at B8 and B9, with B9 providing the clearest response. Thus the defect resonance frequency lies between 27 kHz and 29 kHz for the fundamental and between 54 kHz and 58 kHz for the second harmonic. Sub division of the broad frequency sweep (20–30 kHz fundamental range, 40 kHz and 60 kHz) therefore allows for easy visual assessment of the defect resonance.

Fig. 13 suggest that it is difficult to evaluate the damage between bands B1 and B5 and Fig. 14 suggests that damage detection is only possible at bands B8 and B9.

If bands B1 to B5 are individually normalised it becomes clear that damage is evident at these bands. Which suggests that although these bands do not give the highest relative damage response (defect resonance response) that within these bands there are certain frequencies which do excite various parts of the damage.

In order to assess which band gives the highest defect response the total energy for each band was calculated and normalised, refer to Figs. 16 and 17 below. The total energy was calculated by squaring and integrating the filtered time domain signal for each of the respective frequency bands.

Fig. 16 shows that the highest response occurs between 28 kHz and 29 kHz for the fundamental and between 56 kHz and 58 kHz for the second harmonic. In this case the second harmonic response follows a similar trend to that of the fundamental. There is a complex relationship between the fundamental and the second harmonic response, it would seem obvious to expect the highest second harmonic response to correspond to the highest fundamental response, this is not always the case as defect resonance of the damage between 40 kHz and 60 kHz is not necessarily multiples of the defect resonance between 20 kHz and 30 kHz.

Comparing the damage image for B1 (Fig. 15) to the total relative energy at B1 (Fig. 16), it shows that while B1 gives the lowest response over the frequency range, it is still able to determine the damage location at 10% of the energy when compared to the defect resonance response at B9. This highlights one of the benefits of nonlinear ultrasound methods, sensitivity.

Fig. 17 shows that the highest response occurs between 27–29 kHz and 36–38 kHz for the fundamental and between 54–58 kHz and 72–76 kHz for the second harmonic. The second harmonic results coincide with the highest fundamental frequency bands.

5.2. *Constructive nonlinear array in time (CNAT): Time domain analysis*

The time domain responses of the broad frequency sweep excitation (20–30 kHz for S1 and 20–40 kHz for S2) were captured for all gird points for the 8 excitation locations for the two samples tested. The raw time data for capture position $k = 1$, for each excitation positions j, is highlighted in Fig. 18 for S1. As the time window represents frequencies from 20 kHz (starting at the beginning of the time window) to 30 kHz (towards the end of the time window), it is clear to see that the frequency response and signal amplitude at $k = 1$ is dependent on the location of the excitation position j. These effects can be attributed to directionality and magnitude of the incident wave propagating towards the damage/defect regions and how these are affected by the composite

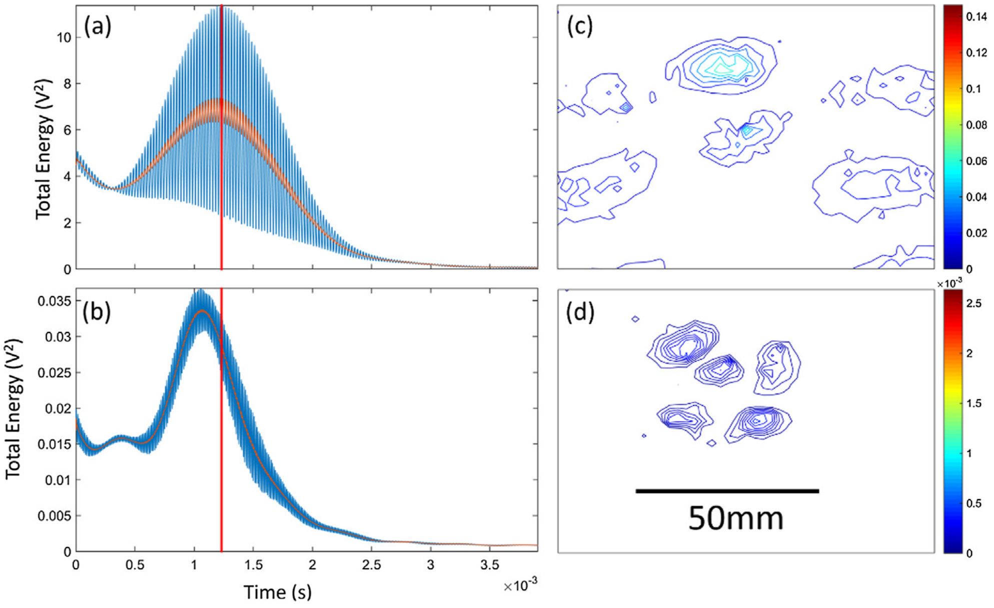

Fig. 24. Fundamental (a) and Second harmonic (b) total energy profile vs. filtered and phase matched image at 0.0012 s (c-Fundamental, d-Second) for sub band B1 (S1: 20–21 kHz).

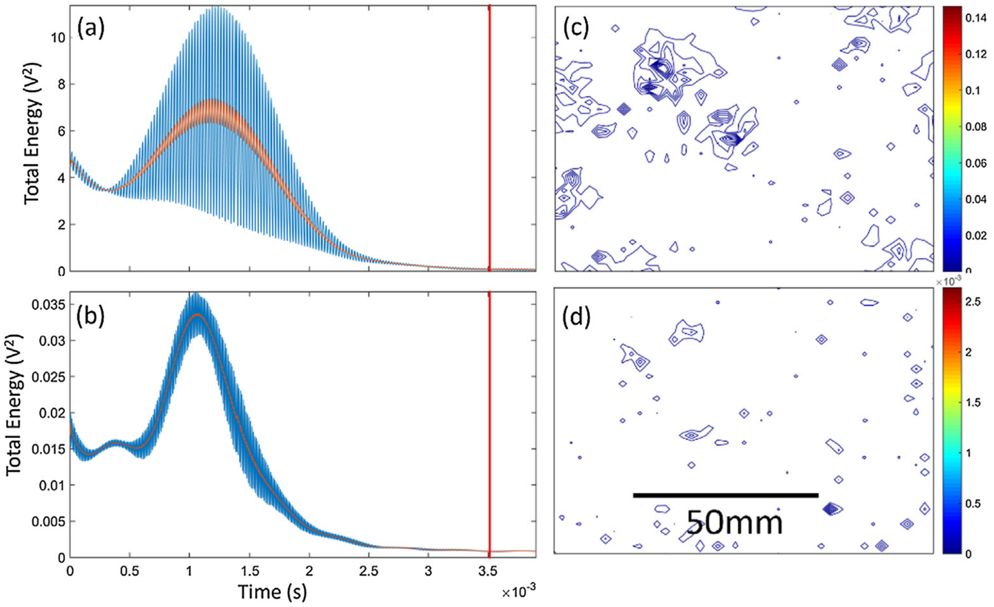

Fig. 25. Fundamental (a) and Second harmonic (b) total energy profile vs. filtered and phase matched image at 0.0013 s (c-Fundamental, d-Second) for sub band B1 (S1: 20–21 kHz).

structures geometry (wave reflections) and mechanical properties i.e. attenuation, the way the wave interacts with boundaries and changes in boundary geometry.

The raw data contains the full frequency responses for both linear and nonlinear elements, in order to deconstruct the signal into the fundamental frequency and harmonic responses filtering over each sub band was conducted. Fig. 19 below shows the filtered signal between 20 kHz and 21 kHz (Fundamental, sub band B1), while Fig. 20 shows the filtered signal between 40 kHz and 42 kHz (Second Harmonic, sub band B1, refer to Table 1), both for S1. The fundamental frequency responses (Fig. 19) show that the energy of the signal is concentrated at the beginning of the signal relating to this bands frequency within the total time signal, while the second harmonic response is much more complicated stretching over the whole time window (Fig. 20). The second harmonic response suggests that if this is a defect response, the defect continues to vibrate after being excited, while the fundamental frequency is limited to the initial wave passing over the damage region and small relative reflections.

The next step in processing required phase matching the 8 individual filtered signals (Eq. (1)) to determine the linear and nonlinear time constructed signals (Fig. 21(a)), then determination of the individual position (k) energy profiles (Fig. 21(b)), and the total energy calculated as the sum of all positions (k) in time (Fig. 21(c)). The second harmonic response are 2–3 orders of magnitude smaller than the fundamental response, this highlights one of the difficulties in accurate and robust nonlinear ultrasound damage assessment. By summing the array results at each k position it is expected that the nonlinear signal to noise ratio (SNR) is magnified considerably when compared to a single excitation system.

Fig. 21(c) shows that there is a distinct peak in the energy profiles

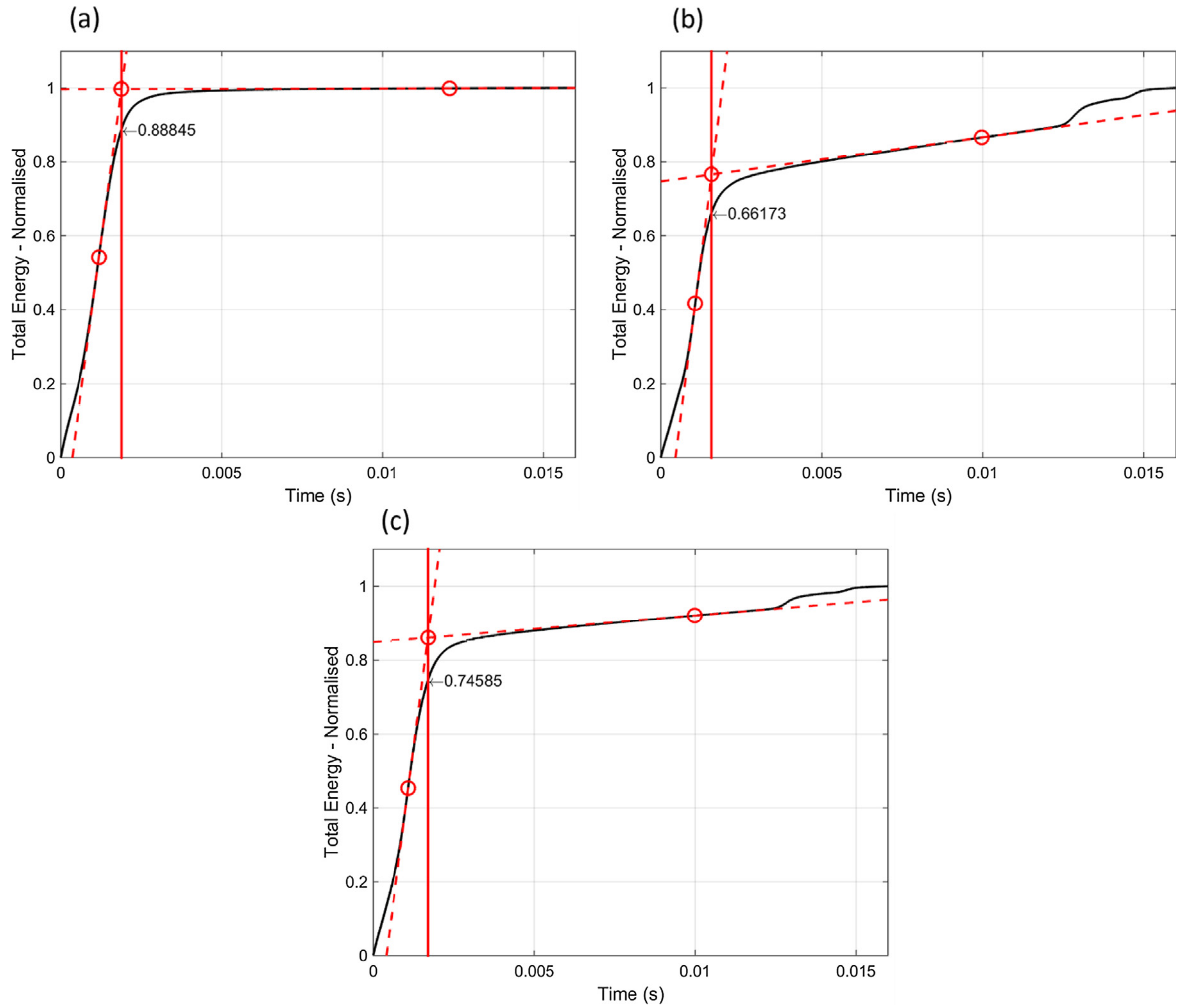

Fig. 26. Determination of time signal cut-off level for damage determination for fundamental frequency (a), second harmonic (b) and combined linear and nonlinear (c) for sub band B1 (S1).

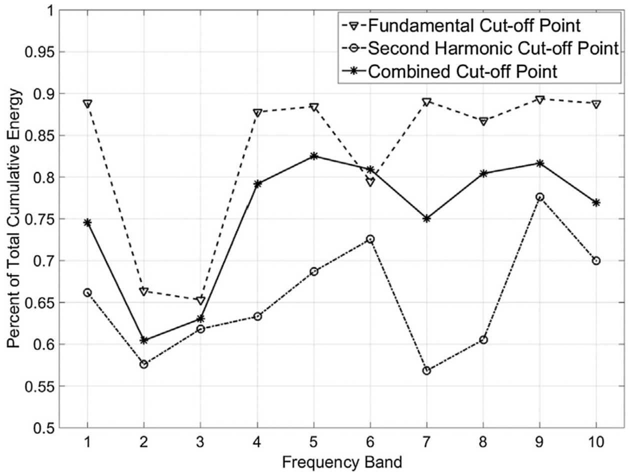

Fig. 27. Cut-off points for damage recognition S1.

for both the fundamental and second harmonic responses in time. From these images it would be possible to determine the frequency at which these peaks occur and in doing so determine the defect resonance frequency between 20 kHz and 21 kHz for B1. All energy profiles for each captured position (*k*) Fig. 21(b) were used to generate an image for each position in time (constructed into a video) in order to evaluate the damage/defect detection capabilities of the method. For the purpose of this report single points in time were reconstructed.

Figs. 22–25 show images of fundamental and second harmonic for three different positions in time. Fig. 22 shows the image relating to 1.1×10^{-3} s with the vertical red line in (a) and (b) relating to the maximum peak of the total second harmonic energy profile (Fig. 21(b) bottom). The line through the middle of the energy response (a) and (b) is the smoothed energy profile. It can be seen that the peak of the total energy profiles for the fundamental and second harmonics are slightly different, and thus relate to different frequencies, again these peaks can be used to determine the defect resonance frequency. Fig. 22(c) shows that the fundamental frequency has a higher response in the damage location but this response is related to excitation of a material mode (with the modes shapes visible either side of the damage region – refer to Fig. 23). In contrast the second harmonic response is only visible at the damage location and clearly identifies the damage region (Fig. 22(d)).

If the fundamental total energy peak is selected as the time of the images (Fig. 24), the damage region becomes clearer as the amplitudes of the mode shapes reduce relative to the location of the damage Fig. 24(c). The second harmonic response Fig. 24(d), clearly only highlights the damage region in a similar manner to Fig. 22(d) although the area has shifted and the region is smaller. The second harmonic shows how different regions within the same damage area can be excited by different frequencies and thus the ability of the sweep methodology to excite the damage region.

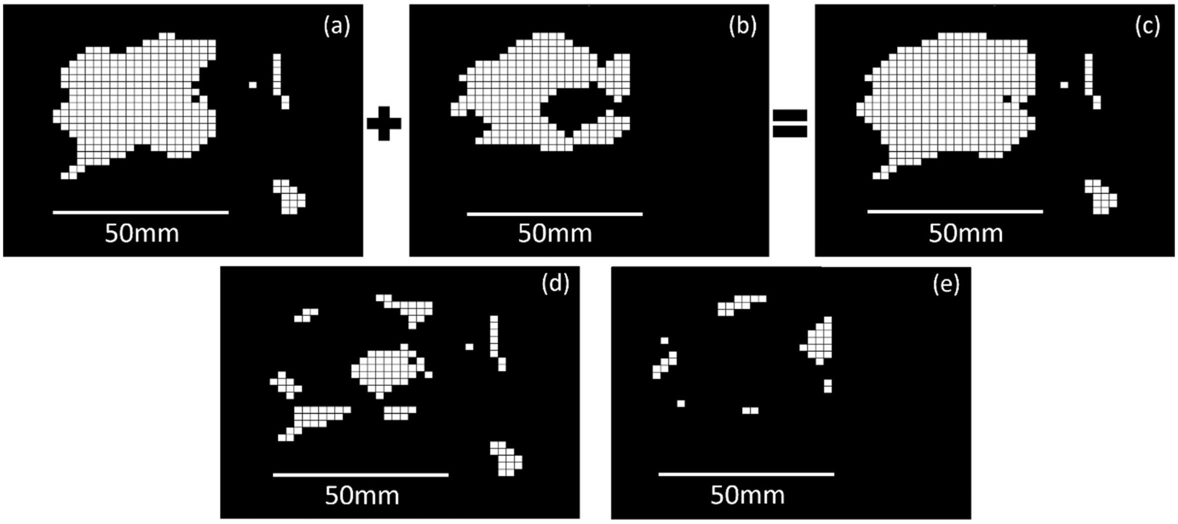

Fig. 28. Damage sizing for sub band B1 (20–21 kHz), fundamental frequency response (a), second harmonic (b), combined linear and nonlinear (c), contribution to combined damaged area from fundamental frequency (d) and contribution to combined damaged area from second harmonic (e) for S1.

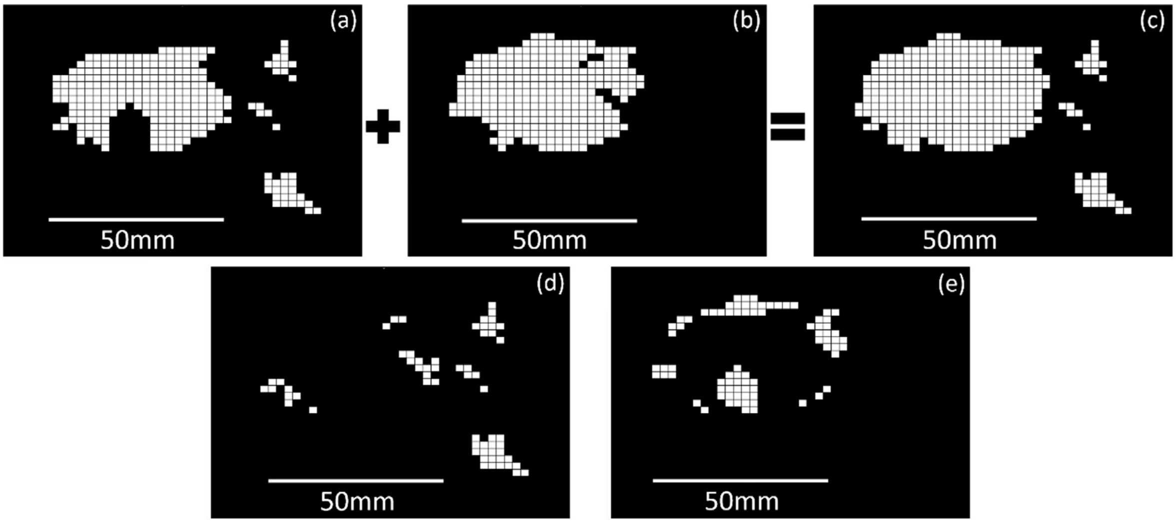

Fig. 29. Damage sizing for sub band B8 (27–28 kHz), fundamental frequency response (a), second harmonic (b), combined linear and nonlinear (c), contribution to combined damaged area from fundamental frequency (d) and contribution to combined damaged area from second harmonic (e) for S1.

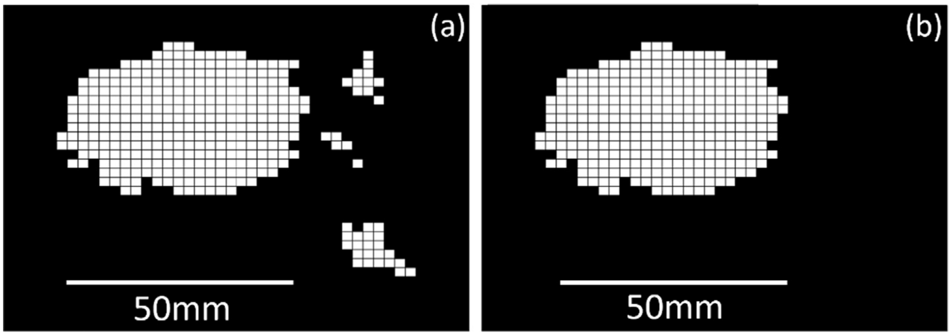

Fig. 30. Damage sizing B8 (27–28 kHz) before (a) and after (b) binary imaging, S1.

If point in time is chosen after the total energy peak, where the energy levels are flat (Fig. 25), it can be seen that there is no clear evidence of damage for both the fundamental (Fig. 25(c)) and second harmonic (Fig. 25(d)), which is expected. The difficulty as pointed out in the Section 2.3 is to develop a methodology that only identifies damage regions, when applying image segmentation (IS) and binary imaging (BI) methods to images (c) and (d) (Fig. 25) large areas will be classified as damage due to the relative amplitude of these points. Most of these points are in fact scattering of noise and will change from frame to frame, thus if an aggregate of all the frames are taken, damage will be perceived to cover the whole inspection area. While this is an issue, the techniques used to determine the final frame to be considered, using

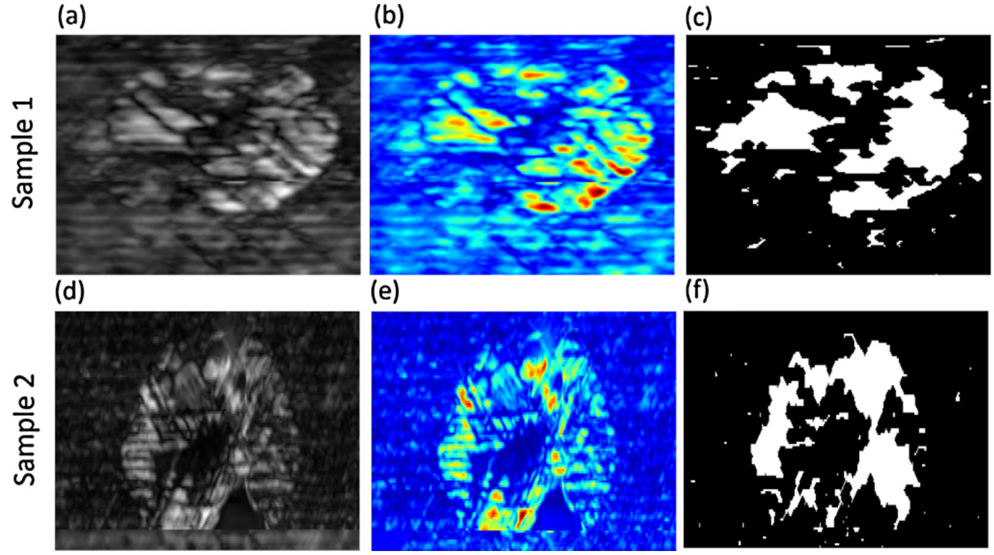

Fig. 31. Impact damage for S1 and S2 – standard phased array amplitude results in grey (a) and (d) and coloured maps (b) and (e), and binary imaging sizing (c, 16.03 cm^2) and (f, 13.90 cm^2).

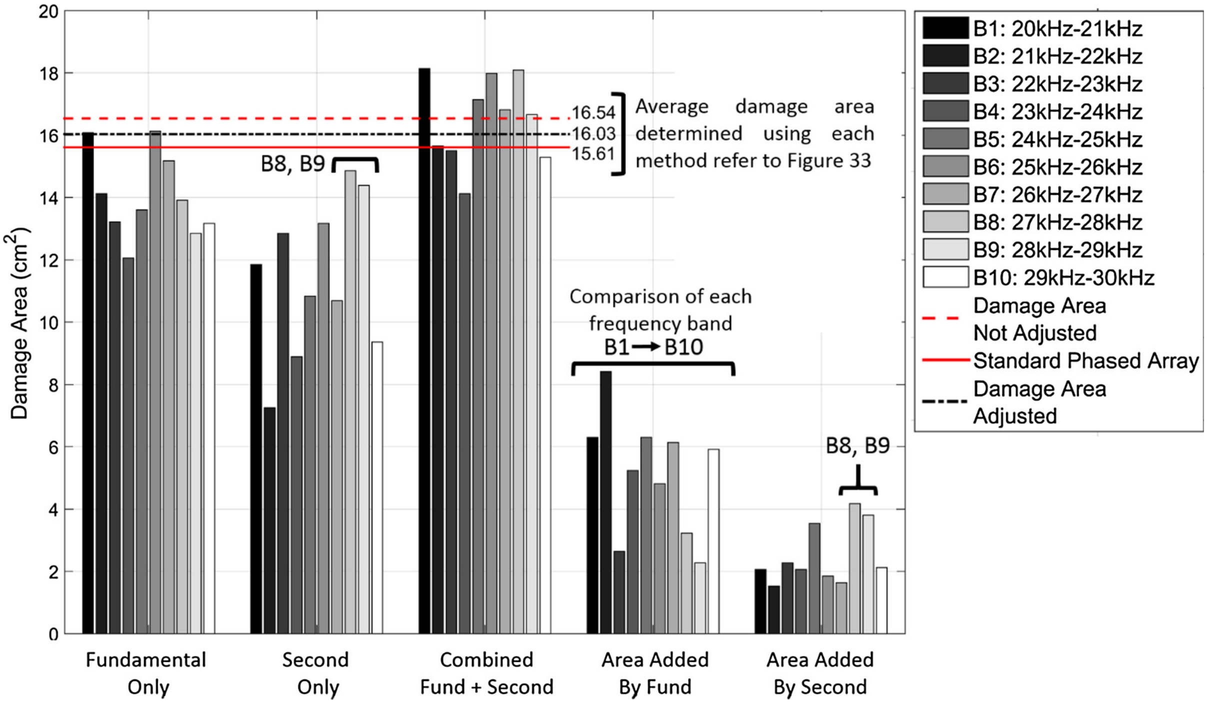

Fig. 32. Summary of damage sizing for each frequency sub band S1.

the max and min gradients of the cumulative energy profile shows good potential to determine the cut-off frame (discussed in the next section).

5.3. CNAT: Damage sizing

The normalised cumulative total energy profiles were determine for the fundamental and second harmonic responses shown in Fig. 26(a) and (b), respectively. Using the methodology of selecting the intersection time between the highest and lowest gradients of the energy profiles it is possible to determine a cut-off point for both the fundamental and second harmonics responses. This cut-off point is used as the last point in time that the image segmentation (IS) algorithm assesses. The fundamental and second harmonic profiles were added together and normalised in order to determine this point for the combined linear and nonlinear results. The main focus of this work is to combine the benefits of linear and nonlinear methods to improve damage detection capabilities. The process of determining the cut-off points was conducted for each frequency sub band evaluated (B1 to B10). The cut-off point percentages of total energy are shown next to the arrows point to the intersection between the cut-off line (red vertical) and the cumulative energy (black line).

Fig. 27 below shows a comparison of the cut-off points between the sub bands as well as between the linear, nonlinear and combined results. As it can be seen the combined cut-off point generally lies in between the fundamental and second harmonic (except for B6). The cut-off methodology is an easily automated and repeatable process.

Once the combined cut-off points for each sub band were determined it was possible to run the IS algorithm to determine the

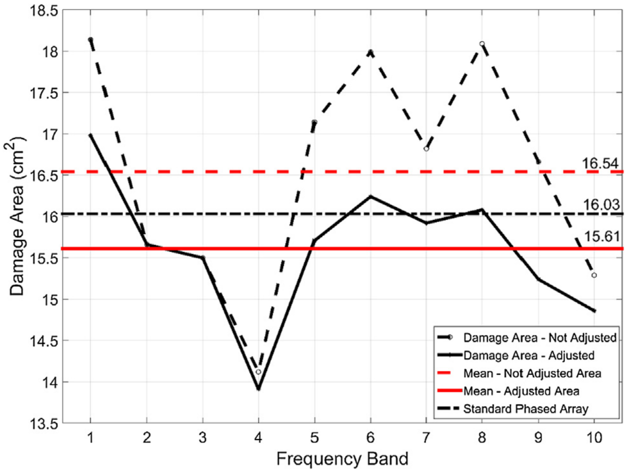

Fig. 33. Damage sizing comparison for each frequency band before and after binary imaging S1.

damage location. Fig. 28 below shows the results for the fundamental response (a), second harmonic (b), the combined (c), damage area added by the fundamental (d) and the damage area added by the second harmonic (e). Images (a) and (b) were simply added to generate the combined image (c), while (d) and (e) show the contribution of each response. For this frequency sub band (B1 – S1) the fundamental response clearly added more to the final image than the second harmonic (nonlinear element). B8 is highlighted and shown in Fig. 29, in this case the second harmonic response contributes more to the overall damage size than the fundamental. These two cases highlight why it is important to consider both the linear and nonlinear responses of a system during non-destructive testing operations.

Comparing Fig. 28(a) with Fig. 23, the two locations to the right of the main damage area seem to fall in the same areas of the fundamental mode shape of the structure while the second harmonic does not show any damage in these regions (the same occurrence can be seen in Fig. 29). This effect shows a false positive damage evaluation by the fundamental when compared with the second harmonic and linear phased array results, justifying the use of the binary imaging method to filter these effects according to the second harmonic.

Fig. 30 below shows damage sizing for B1 (S1) before (a) and after (b) binary imaging (BI) set to the second harmonic response. The process has removed artefacts to the right of the main damage region, which are related to material responses (modal responses) rather than damage.

After determining the damage size for both samples and each frequency band, the standard phased array results were evaluated using the IS method. Fig. 31(c) and (f) show the IS results for S1 and S2, respectively. It is clear that the IS algorithm, in this case, clearly identifies the damage locations (white areas), calculating these regions reveal that S1 has a damage area of $16.03\,\text{cm}^2$ and S2 an area of $13.90\,\text{cm}^2$.

Figs. 32 and 34 show the summarised damage results for samples 1 and 2. The damage response for S1 is dominated by the fundamental frequency as the apparent damage size is generally larger according to the fundamental than the second harmonic, and the fundamental also in most cases provides larger increases in the damage size than the second harmonic. Although, the second harmonic response near the defect resonance frequencies (B8: 27–28 kHz and B9: 28–29 kHz, please refer to Fig. 16) predicts a larger damage than the fundamental and contributes more to the overall size of the damage. This is due to the much reduced nonlinear response (up to 10%) at non-defect resonance frequencies, and the amplification resulting from excitation at defect resonance.

In Figs. 32 and 33, the mean damage size for all frequency bands using the outlined methodology are highlighted with two horizontal lines, one sparsely dotted (higher – $16.54\,\text{cm}^2$ before BI conversion) and the other a solid line (lower – $15.61\,\text{cm}^2$ after BI conversion). A third dotted line (middle – $16.03\,\text{cm}^2$), shows the standard phased array results after IS. As previously suggested the material artefacts (Fig. 30) existing in the unadjusted results (top line) resulted in an overestimate of the damage size by ~3.18% when compared with the standard

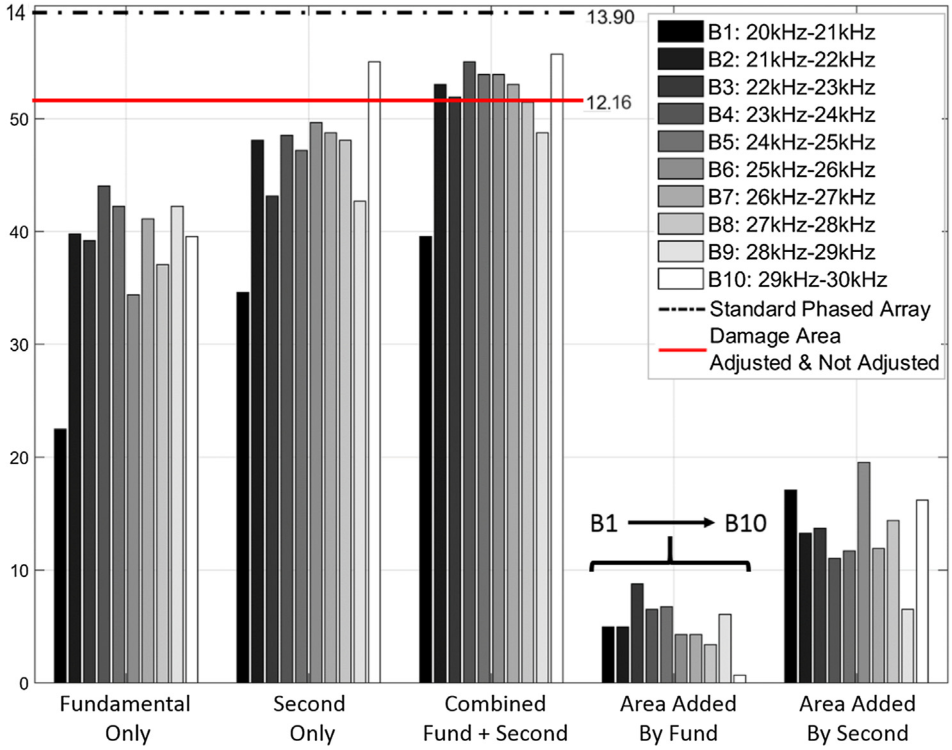

Fig. 34. Summary of damage sizing for each frequency sub band 20 k S2.

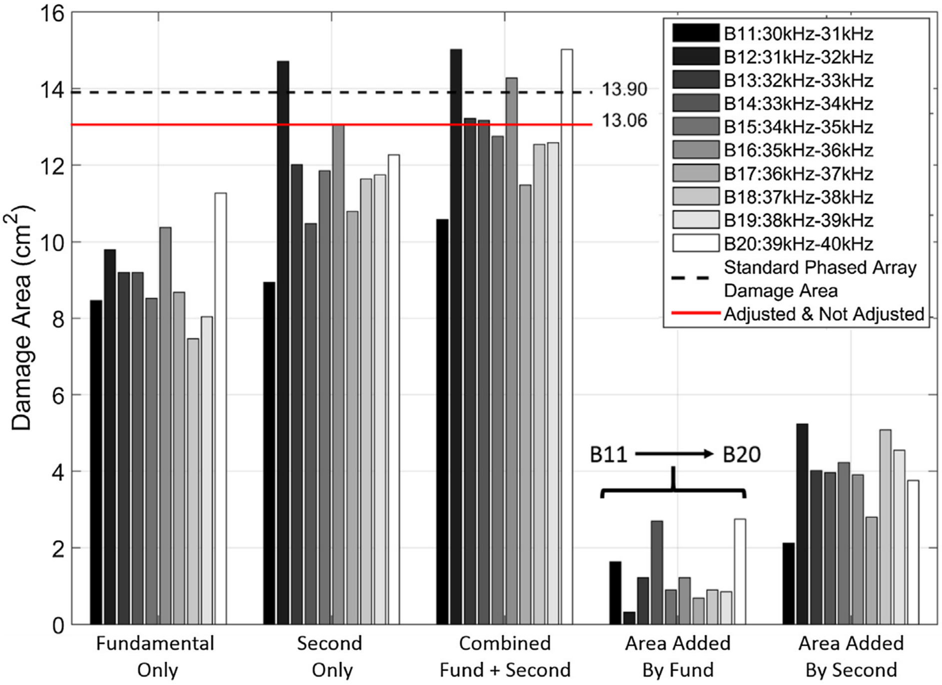

Fig. 35. Summary of damage sizing for each frequency sub band 30 k S2.

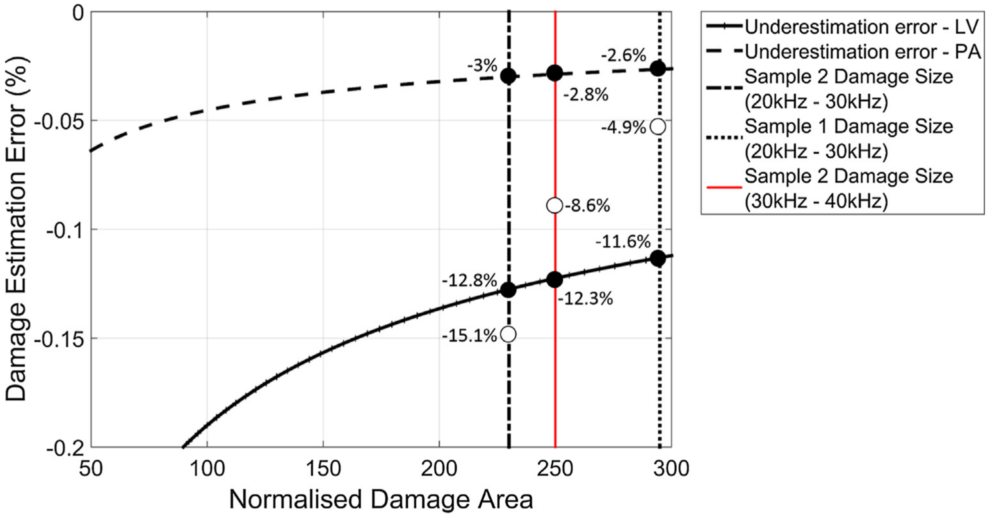

Fig. 36. Damage estimation error for LV and PA for S1 and S2.

Table 3
Damage area errors for S1 (20–30 kHz) and S2 (20–30 kHz and 30–40 kHz).

	Norm. damage area	Error: phased array	Error: laser vibrometer	Max error	Min error
S1 20–30 kHz	295	− 2.6%	− 11.6%	− 4.9%	0.4%
S2 20–30 kHz	230	− 3%	− 12.8%	− 15.1%	− 9.7%
S2 30–40 kHz	250	− 2.8%	− 12.3%	− 8.6%	− 3%

phased array results. Once these artefacts are removed using BI, set according to the second harmonic, there is an underestimate of the damage size of ∼2.62%, thus an improvement in damage evaluation relative to the phased array results.

For S2 (Figs. 34 and 35) the second harmonic response contributes more to damage sizing than the fundamental frequency, unlike S1 (Fig. 32) where the contribution from the fundamental response is larger. Furthermore, for S2, the second harmonic contributes more to the overall size of the damage. The benefit of combining both linear and nonlinear results within a damage detection process is evident as for both samples the damage size increases when the results are combined. The complexity of composites and damage within these materials require multiple damage detection methods to improve the robustness of such methods.

The damage artefacts were not present in the results of S2, thus the adjusted and not adjusted mean damage areas are the same (solid horizontal line, Figs. 34 and 35). For S2 there was a reduction in damage sizing versus the standard phased array technique of ∼12.5%

(20 kHz and 30 kHz) and ~6% (30 kHz and 40 kHz) for the two bands investigated. The fundamental frequency response had a mean damage area of 8.06 cm^2 (20 kHz and 30 kHz) and 9.09 cm^2 (30 kHz and 40 kHz) thus resulting in an underestimation of the damage size of ~33% and ~31% smaller than that of the combine linear and nonlinear estimation and ~42% and ~35% smaller than the phased array results, respectively.

If the damaged areas for S1 and S2 are normalised (dividing by the pitch area, Fig. 36) the maximum damage estimation error can be determined for the LV and PA results. The higher resolution of the PA results in an error of −2.6% for S1 damage and between −2.8% and −3% for S2, while the resolution of the LV results in an error of −11.6% for S1 damage and between −12.3% and −12.8% for S2 damage (when considering the worst case scenario for underestimated error). The deviation of −2.6% for S1 between the LV and PA results, show that the proposed CNAT method provides very good accuracy given the resolution constraints, with an estimated max error of −4.9% (min error of 0.4%, refer to Fig. 36 and Table 3) when adjusting it for the error of the PA. The deviation of −12.5% (20–30 kHz – estimated max error −15.1% and min error −9.7%) for S2, shows that the capture locations for the LV maximised the sizing error. While the −6% error (30–40 kHz – estimated max error −8.6% and min error −3%) for S2 provides a much more accurate estimation of the damage size.

The results for S2 show that defect resonance plays an important role in effective and accurate damage sizing when using the CNAT method. Damage in S2 is smaller than S1 and thus it is expected that a higher frequency will result in better damage evaluation. Furthermore, nonlinear responses have been shown to be more sensitive to smaller damage, evidence for this is shown in Figs. 34 and 35, where a larger damage area was determined when using the second harmonic. This is in direct contrast to the larger damage in S1 which was more sensitive to the fundamental frequency response.

These two opposing results for S1 and S2 can be explained as follows: (1) in S1 the larger damage results in a larger reduction in stiffness over the whole panel which increases the probability that low frequency plate modes will excite the larger damage region (compared to S2, plate modes illustrated in Fig. 23), and (2) due to the smaller damage and thus stiffer panel of S2 low frequency plate modes are not small enough to significantly excite the damage region while the higher sensitivity of the nonlinear effects compensates for these issues. The results suggest that as the damage decreases in size the nonlinear effects should provide more information about the damage size, although the linear contributions, as has been shown Figs. 32, 34 and 35, should not be ignored.

As the damage estimation error falls above the worst case scenario for both S1 and S2 (refer to analytical model, Fig. 36) this suggests that the differences in the sizing between the two methods (PA and LV) is related to resolution differences and that the two methods are comparable with one another. Therefore, using the CNAT method proposed, it is possible to improve damage detection by considering both linear and nonlinear contributions to the damage size, which from the results show that results can be obtained that are equivalent to standard phased array methods.

6. Conclusion

This work provided a framework for semi-contact evaluation and sizing of BVID in composite panels, named CNAT. The method requires fewer excitation and capture locations as the structure is excited with a prolonged lower frequency ultrasonic sweep (inducing steady-state excitation), ultimately increasing the probability of the generation and capture of linear and nonlinear effects produced by damage regions (due to the increased likelihood of exciting at defect resonance). The time domain information was evaluated using a simple thresholding method, before image segmentation and binary imaging were used to evaluate the damage size. The combination of both linear and nonlinear responses in the damage sizing algorithm has shown that there is a clear improvement in sizing accuracy, when compared to the individual linear and nonlinear responses. These results propose that rather than focusing on purely linear or nonlinear NDT/E systems, industry and research bodies should focus on a comprehensive solution incorporating both linear and nonlinear techniques which would have a high impact on improving accuracy, damage detectability and probability of detection. The results suggest, that as damage size reduces the nonlinear responses become the main contributing factor in sizing the damage, although the linear responses should not be ignored. Furthermore, using the nonlinear response as a baseline measure, it was possible to remove damage artefacts relating to material vibration modes thus improving damage sizing accuracy. Finally, a simple analytical model was used to assess the accuracy of the method versus a standard phased array system, which showed that sizing errors between the methods were due to resolution differences and that the methods are comparable.

Acknowledgements

This paper has been funded by the EXTREME project of the European Union's Horizon 2020 research and innovation programme under grant agreement No. 636549.

Appendix A. Supplementary material

Supplementary data to this article can be found online at https://doi.org/10.1016/j.ultras.2018.10.011.

References

[1] P. Stanley, W. Chan, The application of thermoelastic stress analysis techniques to composite materials, J. Strain Anal. Eng. Des. 23 (1988) 137–143.
[2] G. De Angelis, M. Meo, D.P. Almond, S.G. Pickering, S.L. Angioni, A new technique to detect defect size and depth in composite structures using digital shearography and unconstrained optimization, NDT E Int. 45 (2012) 91–96.
[3] I. Solodov, J. Bai, S. Bekgulyan, G. Busse, A local defect resonance to enhance acoustic wave-defect interaction in ultrasonic nondestructive evaluation, Appl. Phys. Lett. 99 (2011) 211911.
[4] G.P.M. Fierro, D. Ginzburg, F. Ciampa, M. Meo, Nonlinear thermosonics and laser vibrometry for barely visible impact damage of a composite stiffener panel, in: T. Yu, A.L. Gyekenyesi, P.J. Shull, H.F. Wu, Hg (Eds.), SPIE smart structures and materials+ Nondestructive Evaluation and Health Monitoring, United States, Nevada, 2016, p. 980419.
[5] D. Dionysopoulos, G.P.M. Fierro, M. Meo, F. Ciampa, Imaging of barely visible impact damage on a composite panel using nonlinear wave modulation thermography, NDT E Int. (2018).
[6] G.P.M. Fierro, M. Meo, Nonlinear imaging (NIM) of flaws in a complex composite stiffened panel using a constructive nonlinear array (CNA) technique, Ultrasonics (2016).
[7] W. Morris, O. Buck, R. Inman, Acoustic harmonic generation due to fatigue damage in high strength aluminum, J. Appl. Phys. 50 (2009) 6737–6741.
[8] A.J. Hillis, S.A. Neild, B.W. Drinkwater, P.D. Wilcox, Global crack detection using bispectral analysis, Proc. Roy. Soc. A: Math. Phys. Eng. Sci. 462 (2006) 1515.
[9] D.M. Donskoy, A.M. Sutin, Vibro-acoustic modulation nondestructive evaluation technique, J. Intell. Mater. Syst. Struct. 9 (1998) 765.
[10] S. Boccardi, D. Calla, G.-P. Fierro, F. Ciampa, M. Meo, Nonlinear damage detection and localisation using a time domain approach, Struct. Health Monitor. 2015 (2015).
[11] G.P.M. Fierro, M. Meo, SPIE smart structures and materials+ nondestructive evaluation and health monitoring, Int. Soc. Opt. Photon. (2017) pp. 1017009-1017009-1017010.
[12] J.H. Cantrell, W.T. Yost, Nonlinear ultrasonic characterization of fatigue microstructures, Int. J. Fatigue 23 (2001) 487–490.
[13] G.P.M. Fierro, D. Ginzburg, F. Ciampa, M. Meo, Nonlinear ultrasonic stimulated thermography for damage assessment in isotropic fatigued structures, J. Sound Vib. 404 (2017) 102–115.
[14] G.P.M. Fierro, M. Meo, Identification of the location and level of loosening in a multi-bolt structure using nonlinear ultrasound, Struct. Health Monitor. 2017 (2017).
[15] D. Dutta, H. Sohn, K.A. Harries, P. Rizzo, A nonlinear acoustic technique for crack detection in metallic structures, Struct. Health Monitor. Int. J. 8 (2009) pp. 573-573.
[16] G.M. Fierro, F. Ciampa, D. Ginzburg, E. Onder, M. Meo, Nonlinear ultrasound modelling and validation of fatigue damage, J. Sound Vib. 343 (2015) 121–130.
[17] G.P.M. Fierro, M. Meo, Residual fatigue life estimation using a nonlinear ultrasound

modulation method, Smart Mater. Struct. 24 (2015) 025040.
[18] T. Ulrich, P.A. Johnson, R.A. Guyer, Interaction dynamics of elastic waves with a complex nonlinear scatterer through the use of a time reversal mirror, Phys. Rev. Lett. 98 (2007) 104301.
[19] R.A. Guyer, P.A. Johnson, Nonlinear mesoscopic elasticity: Evidence for a new class of materials, Phys. Today 52 (1999) 30–36.
[20] M. Meo, G. Zumpano, Nonlinear elastic wave spectroscopy identification of impact damage on a sandwich plate, Compos. Struct. 71 (2005) 469–474.
[21] F. Ciampa, S. Pickering, G. Scarselli, M. Meo, Health Monitoring of Structural and Biological Systems 2014, International Society for Optics and Photonics, 2014 906402.
[22] M. Scalerandi, A. Gliozzi, C.L.E. Bruno, D. Masera, P. Bocca, A scaling method to enhance detection of a nonlinear elastic response, Appl. Phys. Lett. 92 (2008) 101912.
[23] L. Straka, Y. Yagodzinskyy, M. Landa, H. Hänninen, Detection of structural damage of aluminum alloy 6082 using elastic wave modulation spectroscopy, NDT E Int. 41 (2008) 554–563.
[24] K.-A. Van Den Abeele, P.A. Johnson, A. Sutin, Nonlinear elastic wave spectroscopy (NEWS) techniques to discern material damage, part I: nonlinear wave modulation spectroscopy (NWMS), J. Res. Nondestruct. Eval. 12 (2000) 17–30.
[25] G.P.M. Fierro, M. Meo, Nonlinear imaging (NIM) of flaws in a complex composite stiffened panel using a constructive nonlinear array (CNA) technique, Ultrasonics 74 (2017) 30–47.
[26] G.-P.M. Fierro, F. Pinto, S.D. Iacono, A. Martone, E. Amendola, M. Meo, Monitoring of self-healing composites: a nonlinear ultrasound approach, Smart Mater. Struct. 26 (2017) 115015.
[27] S. Dos Santos, Z. Prevorovsky, Imaging of human tooth using ultrasound based chirp-coded nonlinear time reversal acoustics, Ultrasonics 51 (2011) 667–674.
[28] F. Ciampa, M. Meo, Nonlinear elastic imaging using reciprocal time reversal and third order symmetry analysis, J. Acoust. Soc. Am. 131 (2012) 4316–4323.
[29] A. Sugawara, K. Jinno, Y. Ohara, K. Yamanaka, Closed-crack imaging and scattering behavior analysis using confocal subharmonic phased array, Jpn. J. Appl. Phys. 54 (2015) pp. 07HC08.
[30] Y. Ohara, T. Mihara, R. Sasaki, T. Ogata, S. Yamamoto, Y. Kishimoto, K. Yamanaka, Imaging of closed cracks using nonlinear response of elastic waves at subharmonic frequency, Appl. Phys. Lett. 90 (2007) 011902.
[31] J. Potter, A. Croxford, P. Wilcox, Nonlinear ultrasonic phased array imaging, Phys. Rev. Lett. 113 (2014) 144301.
[32] C.-S. Park, J.-W. Kim, S. Cho, D.-C. Seo, A high resolution approach for nonlinear sub-harmonic imaging, NDT E Int. 79 (2016) 114–122.
[33] B. Kang, P. Cawley, Review of Progress in Quantitative Nondestructive Evaluation, AIP Publishing, 2007, pp. 484–491.
[34] S. Pickering, K. Chatterjee, D. Almond, S. Tuli, LED optical excitation for the long pulse and lock-in thermographic techniques, NDT E Int. 58 (2013) 72–77.
[35] G.P.M. Fierro, D. Ginzburg, F. Ciampa, M. Meo, Imaging of barely visible impact damage on a complex composite stiffened panel using a nonlinear ultrasound stimulated thermography approach, J. Nondestr. Eval. 36 (2017) 69.
[36] G. Sun, Z. Zhou, Non-contact detection of delamination in layered anisotropic composite materials with ultrasonic waves generated and detected by lasers, Optik-Int. J. Light Electron Opt. 127 (2016) 6424–6433.
[37] M. Martarelli, P. Chiariotti, M. Pezzola, P. Castellini, AIP Conference Proceedings, AIP, 2014, pp. 405–412.
[38] A. Karabutov, N. Podymova, Quantitative analysis of the influence of voids and delaminations on acoustic attenuation in CFRP composites by the laser-ultrasonic spectroscopy method, Compos. B Eng. 56 (2014) 238–244.
[39] M. Castaings, P. Cawley, The generation, propagation, and detection of Lamb waves in plates using air-coupled ultrasonic transducers, J. Acoust. Soc. Am. 100 (1996) 3070–3077.
[40] S.P. Kelly, R. Farlow, G. Hayward, Applications of through-air ultrasound for rapid NDE scanning in the aerospace industry, IEEE Trans. Ultrason. Ferroelectr. Freq. Control 43 (1996) 581–591.
[41] T. Gan, D. Hutchins, D. Billson, D. Schindel, The use of broadband acoustic transducers and pulse-compression techniques for air-coupled ultrasonic imaging, Ultrasonics 39 (2001) 181–194.
[42] R. Kažys, A. Demčenko, E. Žukauskas, L. Mažeika, Air-coupled ultrasonic investigation of multi-layered composite materials, Ultrasonics 44 (2006) e819–e822.
[43] J.T. Case, S. Kharkovsky, R. Zoughi, G. Steffes, F.L. Hepburn, AIP Conference Proceedings, AIP, 2008, pp. 970–975.
[44] D.K. Hsu, K.-S. Lee, J.-W. Park, Y.-D. Woo, K.-H. Im, NDE inspection of terahertz waves in wind turbine composites, Int. J. Precis. Eng. Manuf. 13 (2012) 1183–1189.
[45] P. Lambrineas, J. Davis, B. Suendermann, P. Wells, K. Thomson, R. Woodward, G. Egglestone, K. Challis, X-ray computed tomography examination of inshore minehunter hull composite material, NDT E Int. 24 (1991) 207–213.
[46] C. Liu, L. Cheng, X. Luan, W. Zhang, C. Wang, Real-time damage evaluation of a SiC coated carbon/carbon composite under cyclic fatigue at high temperature in an oxidizing atmosphere, Mater. Sci. Eng., A 524 (2009) 98–101.